

ADA053195

DAMAGE PROFILES IN SILICON AND THEIR
IMPACT ON DEVICE RELIABILITY

(P) (9)

G. H. Schwuttke, Principal Investigator, 914 - 897-3140

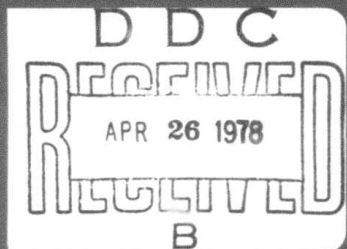
International Business Machines Corporation
East Fishkill Laboratories
Hopewell Junction, New York 12533

Final Report
April 1, 1978

prepared by

G. H. Schwuttke and K. H. Yang

Contract No. N00173-76-C-0303
Effective Date of Contract: 10/1/76
Contract Expiration Date: 4/1/78



Sponsored by

Advanced Research Projects Agency (DOD)
ARPA Order No. 3231, Program Code No. 6D10
Form approved budget bureau No.: 22-R0293

The views and conclusions contained in this document are those of the authors and should not be interpreted as necessarily representing the official policies, either expressed or implied, of the Defense Advanced Research Projects Agency (DOD) or the U. S. Government.

DISTRIBUTION STATEMENT A

Approved for public release;
Distribution Unlimited

UNCLASSIFIED

(11) 1 Apr 78

SECURITY CLASSIFICATION OF THIS PAGE (When Data Entered)

REPORT DOCUMENTATION PAGE		READ INSTRUCTIONS BEFORE COMPLETING FORM
1. REPORT NUMBER	2. GOVT ACCESSION NO.	3. RECIPIENT'S CATALOG NUMBER

4. TITLE (and Subtitle)	5. TYPE OF REPORT & PERIOD COVERED
DAMAGE PROFILES IN SILICON AND THEIR IMPACT ON DEVICE RELIABILITY.	Final Report Oct [redacted] 76-Feb [redacted] 78

6. AUTHOR(s)	7. PERFORMING ORG. REPORT NUMBER
G. H. Schwuttke [redacted] K. H. Yang	TR-22.2185

8. CONTRACTOR OR GRANT NUMBER(s)	new
9. PERFORMING ORGANIZATION NAME AND ADDRESS	10. PROGRAM ELEMENT, PROJECT, TASK AREA & WORK UNIT NUMBERS
IBM CORPORATION System Products Division, E ⁶⁵ , Fishkill Labs. Hopewell Junction, New York 12533	Program Element No. 61101E Program Code No. 6D10 DARPA Order No. 3231

11. CONTROLLING OFFICE NAME AND ADDRESS	12. REPORT DATE
Advanced Research Projects Agency Materials Sciences Office 1400 Wilson Blvd., Arlington, Virginia 22209	April 1, 1978
14. MONITORING AGENCY NAME & ADDRESS (if different from Controlling Office)	13. NUMBER OF PAGES
Naval Research Laboratory Code 5261, P. R. Reid Washington, D.C. 20375	135 (12) 152p
	15. SECURITY CLASS (of this report)
	Unclassified
	15a. DECLASSIFICATION/DOWNGRADING SCHEDULE

16. DISTRIBUTION STATEMENT (of this Report)	D D C REFINED APR 26 1978 RELEASER B
17. DISTRIBUTION STATEMENT (of the abstract entered in Block 20, if different from Report)	

18. SUPPLEMENTARY NOTES	
-------------------------	--

19. KEY WORDS (Continue on reverse side if necessary and identify by block number)	
Energy Loss Spectra Analysis Epitaxy Gallium Arsenide Gettering	Oxygen Precipitation Silicon

20. ABSTRACT (Continue on reverse side if necessary and identify by block number)	
The principle of defect engineering is applied to GaAs substrates to produce epitaxial layers of low crystallographic defect density. Defect engineering is achieved through control of surface stresses in GaAs wafers during high temperature processing. Surface stress control is obtained through Impact Sound Stressing damage introduced on wafer backsides before epitaxial processing. Thus, epitaxial GaAs layers obtained through liquid phase epitaxy contain low dislocation numbers through confinement of threading dislocations to the epitaxial-substrate interface.	
A detailed analysis of ISS damage in GaAs before and after annealing is also given.	

CONTENTS

	<u>Page</u>
INTRODUCTION	v
Summary of Significant Accomplishments	viii
Presentations and Publications	xiii
 Chapter 1	
CHARACTERIZATION AND APPLICATION OF IMPACT SOUND	
STRESSING DAMAGE IN GaAs	1
 INTRODUCTION	1
EXPERIMENTAL	2
RESULTS	4
Damage in GaAs: As-Stressed	4
Compressive Damage	4
Abrasive Damage	10
Damage in GaAs: Annealed	12
The Influence of ISS Damaged Substrates on	
Epitaxial Quality	23
DISCUSSION	27
SUMMARY	35
ACKNOWLEDGMENTS	36
REFERENCES	37

BY _____		
DISTRIBUTION/AVAILABILITY CODES		
Dist.	AVAIL	and/or SPECIAL
A		-

	<u>Page</u>
Chapter 2	
DIRECT IDENTIFICATION OF OXIDE PRECIPITATES IN ANNEALED SILICON CRYSTALS	40
INTRODUCTION	40
EXPERIMENTAL	41
RESULTS AND DISCUSSION	42
CONCLUSION	48
REFERENCES	49
APPENDIX I	
Table of Contents of Reports Published	50
APPENDIX II(a)	
Impact Sound Stressing of GaAs Wafers	70
APPENDIX II(b)	
Depth of Damage Induced in GaAs by Impact Sound Stressing	108

INTRODUCTION

This Final report consists of two chapters. Chapter 1 summarizes the contract work on GaAs. The principle of "defect engineering" is applied to GaAs substrates to produce epitaxial layers of low crystallographic defect density. Defect engineering is achieved through control of surface stresses in GaAs wafers during high temperature processing. Surface stress control is obtained through Impact Sound Stressing damage introduced on wafer backsides before epitaxial processing. Thus, epitaxial GaAs layers grown through liquid phase epitaxy contain low dislocation numbers through confinement of threading dislocations to the epitaxial-substrate interface. A detailed analysis of ISS damage in GaAs before and after annealing is also given.

Chapter 2 completes the work on the influence of oxygen on minority carrier lifetime. (See Techn. Report No. 2, published Oct. 1977). Using electron energy loss spectra of precipitates formed in annealed silicon the precipitates are directly analyzed (for the first time) and shown to consist of oxygen and silicon.

This Final report concludes a five year study of the mechanical damage present in semiconductor wafers and its influence on semiconductor device properties specifically minority carrier lifetime.

The accomplishments of the total ARPA contract work are documented in ten (10) major technical reports. Tables of Content of these reports are given in Appendix I. Major accomplishments under the contract relate to the reduction of leakage currents in high performance, high density semiconductor devices and are listed in the section entitled: Summary of Significant Accomplishments.

One outstanding result of this pioneering contract work is that it focused attention on residual damage distribution present in silicon wafers after slicing and polishing, and its impact on yield and reliability of high performance integrated silicon devices. Previously, silicon wafers were assumed to be crystallographically perfect after polishing. The fundamental importance of the "damage profile" existing in a polished silicon wafer and its impact on leakage currents and device yield was established.

Another important result of this contract work relates to the concept of "defect engineering" which leads to the

introduction of the "predamaged" semiconductor wafer. It was demonstrated under ARPA contract that mechanical damage and resulting crystallographic defects can be used as "gettering sites" to reduce leakage in high performance semiconductor devices.

Today, many of the concepts pioneered in this work are now widely accepted and applied throughout the semiconductor industry.

Summary of Significant Accomplishments Under ARPA Contracts

1. Introduction of the "predamaged" wafer concept to achieve "gettering" and thus higher yield during semiconductor device processing.
2. Significant lifetime improvements in silicon obtained after high temperature processing of silicon wafers ISS'ed on the wafer backside.
3. Significant lifetime improvements obtained in epitaxial layers grown on substrates ISS'ed on wafer backside.
4. The effectiveness of modern silicon polishing technique was measured in terms of damage removal.
5. It was established that standard polishing techniques - as used in semiconductor industry - can vary considerably in mechanical damage removal effectiveness and that no polishing technique can recover the initial lifetime of minority carriers in silicon surfaces completely.
6. The chem.-mech. silicon-dioxide polishing technique was shown to be most successful in re-establishing lifetime

in mechanically damaged silicon surfaces.

7. Through a complete analysis of low temperature mechanical deformation of silicon it was shown that shear loops and micro-splits are introduced into silicon wafers.
8. The detrimental effect of micro-splits (residual mechanical damage) present in silicon wafers on carrier lifetime was established.
9. Micro-splits were identified as nucleation centers for oxidation induced stacking faults.
10. The influence of oxidation induced stacking faults on minority carrier lifetime was established (in silicon wafers and epitaxial silicon).
11. A systematic approach for characterizing ID sawing procedures of silicon crystals was developed. The practice relies on damage profiles obtained from sliced wafers. The damage profiles are obtained through the evaluation of x-ray topographs of sliced wafers. It was shown that such damage profiles are useful in describing the entire slicing procedure of a crystal.

This approach removes much of the difficulty encountered previously in achieving reproducible results of saw damage measurements. For the purpose of process improvements the damage profile method can be used advantageously to optimize sawing parameters.

12. The technique of Hertzian fracture cones was applied to the investigation of fracture strength of silicon and its variation, from seed to tail. Quantitative data were obtained by evaluating cone fractures through x-ray transmission topography. Thus a convenient and very sensitive method was found for obtaining a measure of cone depth and cone base projections. The major results of this investigation is that the seed part of a Czochralski crystal is mechanically stronger than the tail part. Thus seed part wafers are less susceptible to saw damage during slicing.
13. Investigations related to the damage distribution in virgin silicon wafers before and after oxidation resulted in the discovery of micro-splits and their detrimental influence on lifetime. The micro-splits were shown to be related to residual saw damage.
14. Micro-splits reduction in silicon surfaces after ID

- slicing was achieved by minimizing active shear forces in the (111) slip planes of the wafer during slicing.
15. Micro-split reduction experiments led to the discovery that the <115> crystal orientation has an interesting potential for device application.
 16. Other important influences on the reduction of residual saw damage in silicon wafer surfaces were shown to be: The speed of crystal slicing and the polishing technique.
 17. The detrimental influence of stacking faults, crystal contamination and dislocations on generation-lifetime was established.
 18. The method of impact sound stressing (ISS) was successfully applied to produce micro-splits in silicon wafers in a controlled way; thus the influence of mechanical damage on lifetime properties could be measured.
 19. The influence of oxygen on the minority carrier lifetime of silicon was studied. It was found that bulk annealed, oxygen-rich crystals subsequently sliced into wafers show lifetime degradation proportional to

anneal time. Silicon oxide precipitates and punched out dislocation loops induced during annealing were identified as electrically active defects responsible for lifetime degradation. Increase in device yields (diodes) and improved lifetime in epitaxial films obtained with oxygen-rich wafers as substrates were shown to be a result of "intrinsic gettering" of oxygen-rich wafers. It was shown that "external gettering" cannot improve minority carrier lifetime in silicon wafers if during processing "intrinsic gettering" is activated. It was also shown that "external gettering" such as impact sound stressing (ISS) is very effective in improving lifetime for wafers not containing "intrinsic gettering" sources.

20. For the first time "direct" evidence was produced that precipitation in annealed oxygen rich silicon crystals consist of oxygen and silicon.
21. The ISS technique was applied to GaAs wafers.
22. Epitaxial layers on GaAs substrates of lower defect density were obtained after liquid phase epitaxy on ISS stressed substrates.

Presentations and Publications under ARPA Contracts

- 1) "Microsplits in Silicon Surfaces", by G. H. Schwuttke and E. Hearn, presented at the Electrochem. Soc. Meeting, Chicago, May 1973.
- 2) "Crystal Damage and Bulk Lifetime", by G. H. Schwuttke, invited paper International Conference FSDERC, Munich, September 1973.
- 3) "The Closed Boat - A New Approach to Slip-Free Batch Processing of Silicon Wafers", by E. Hearn, E. teKaat, and G. H. Schwuttke, Semiconductor Symposium of Electrochem. Soc., San Francisco, May 1974.
- 4) "Requirements for Long Lifetime Silicon Wafers", by G. H. Schwuttke, invited paper at Solar Energy Symp., Tuscon, Arizona, May 1974.
- 5) "Silicon Material Processing Problems", by G. H. Schwuttke, invited lecture at the Summer Schools on Scientific Principles in Semiconductor Technology, Bad Boll, Germany, July 1974.

- 6) "Silicon Materials Processing Problems", by G. H. Schwuttke, invited paper at NSF Review Meeting, Pasadena, Calif., June 1974.
- 7) "Materials Problems in LSI-Technology", by G. H. Schwuttke, invited paper at IEEE Solid State Circuit Committee Workshop: Semiconductor Manufacturing Technology, September 4, 1974, Asilomar, Calif.
- 8) "Characterization of Silicon", by G. H. Schwuttke, opening paper German National X-Ray Topography Meeting, Oct. 1975, Aachen, Germany.
- 9) "Stacking Fault Generation in Impact Sound Stressing Silicon," H. F. Kappert, G. H. Schwuttke and K. H. Yang, Electrochem. Soc. Meeting, Toronto, Canada, Oct. 1975.
- 10) Seminar: "Materials Problem in LSI", by G. H. Schwuttke conducted at the National Broadcasting Laboratories, Tokyo, Japan, Dec. 2, 1975.
- 11) Seminar: "Lifetime Problems in Silicon", by G. H. Schwuttke conducted at the Solid State Physics Lab., Ministry of Defense, New Delhi, India, Dec. 6, 1975.

- 12) "X-Ray Topography", by G. H. Schwuttke, published in Epitaxial Growth, Academic Press, 1975, pg. 281 (edited by J. W. Matthews).
- 13) "Silicon Material Processing Problems," by G. H. Schwuttke, published in Proceedings of Summer Schools, Bad Boll, West Germany, (1975).
- 14) "Long Lifetime Silicon Requirements," by G. H. Schwuttke, published in Proceedings Solar Energy Symposium, Tuscon, Arizona (1975).
- 15) "Stacking Faults and 90° Dislocations in Silicon Produced Through Surface Damage", by H. F. Kappert, G. H. Schwuttke, and K. H. Yang; paper presented at the Spring Meeting of the German Phys. Soc. Meeting, March 1976.
- 16) Silicon Deformation at Room Temperature by K. Yang, G. H. Schwuttke, H. F. Kappert; paper presented at the 1976 Electronics Material Conf., June 23, 1976, Salt Lake City, Utah.
- 17) "Technology's Energy Promise", by G. H. Schwuttke, keynote address, Data Processing Seminar, June 23, 1976, Christchurch, New Zealand.

- 18) "Improvement of Lifetime Properties in Silicon", by G. H. Schwuttke; opening paper at the 1st Japanese Congress on Materials Science, Tokyo, July, 1976.
- 19) "Impact Sound Stressing of Silicon: A New Technique to Improve Minority Carrier Lifetime", by G. H. Schwuttke, invited paper at the IEEE workshop March Meeting, 1977, Washington, D.C.
- 20) "Minority Carrier Lifetime Control and Defect Structure in Silicon after Cesium Implantation", by G. Sixt, H. F. Kappert and G. H. Schwuttke, presented at the International Symposium on Solid State Device Technology, Muenster, West Germany, March 8, 1977.
- 21) "The Influence of Residual Ion Damage on Minority Carrier Lifetime after Ar⁺ and Si⁺ Implantation", by H. F. Kappert, G. Sixt and G. H. Schwuttke, presented at the International Symposium on Solid State Device Technology, Muenster, West Germany, March 8, 1977.
- 22) "Lifetime Control in Si Through Impact Sound Stressing", by G. H. Schwuttke, K. H. Yang and H. F. Kappert. Presented at the International Symposium on Solid State Device Technology, Muenster, West-Germany, March 8, 1977.

- 23) "Lifetime Control in Silicon through Impact Sound Stressing (ISS)", by G. H. Schwuttke and K. H. Yang, Invited Paper at the 19th Electronic Materials Meeting, Cornell University, Ithaca, New York, June 29, 1977.
- 24) "Application of Synchrotron Radiation to X-ray Topography": on an international workshop held at Cornell University, July 29, 1977; opening paper presented by G. H. Schwuttke, at the German X-ray topography meeting, Munich, West-Germany, October 14, 1977.
- 25) "Lifetime Control in Silicon through Impact Sound Stressing", by G. H. Schwuttke, K. H. Yang, and H. F. Kappert, published in phys. stat. sol. (a) 42, 553, 1977.
- 26) "Minority Carrier Lifetime and Defect Structure in Silicon After Cesium Implantation", by G. Sixt, H. F. Kappert, and G. H. Schwuttke, published in phys. stat. sol. (a) 43, August, 1977.
- 27) "Lifetime Control in Silicon through Impact Sound Stressing", by G. H. Schwuttke and K. H. Yang, Am. Phys. Soc. Meeting, Miami, Fla., Nov. 21, 1977.

Chapter 1

CHARACTERIZATION AND APPLICATION OF IMPACT SOUND STRESSING DAMAGE IN GaAs

by K. H. Yang and G. H. Schwuttke

INTRODUCTION

The detrimental impact of wafer surface damage on the electronic properties of semiconductor crystals such as silicon, GaAs and others is well known. Numerous workers in the field have studied damage in semiconductor crystals caused by grinding, polishing or lapping. A summary of this work was given in ARPA Report No. 3 of this contract (1). Due to the complexity of damage introduced during surface preparation of semiconductor crystals, specifically GaAs, an analysis of crystal damage is difficult. Consequently, surface damage in GaAs before and after annealing is not well understood and warrants further investigations.

Recently, the technique of Impact Sound Stressing (ISS) has been shown to be very useful in the study of mechanical damage in a silicon surface (2). This technique has found unique utilization not only in degrading silicon surfaces in

a controlled manner, and thus allowing detailed damage studies, but also in using mechanical damage, introduced on the wafer backside, to reduce the defect density in the wafer frontside during high temperature processing through damage gettering.

The use of backside damage as gettering sites has been shown to be very effective in silicon by several workers (2-6). In those studies damage was introduced by means of mechanical (2-4) or ion implantation techniques (5,6). In GaAs, only ion implantation damage gettering has been shown to be applicable (7).

The purpose of this study is to apply ISS to GaAs wafers, study the characteristics of ISS damage in GaAs and its concomitant possible gettering effect. The damage is studied as-introduced (at room temperature) and after annealing during epitaxial growth. The influence of the gettering action of ISS damage on backsides of GaAs substrates on crystal perfection of epitaxial GaAs layers grown on such substrates is also investigated.

EXPERIMENTAL

GaAs wafers used are doped with tin ($\text{Sn} \sim 6.5 \times 10^{17}$ atoms/cm³) to a resistivity of 0.0035 Ω-cm. The surface of

these wafers is in the (100) orientation. The Impact Sound Stressing (ISS) technique previously used for silicon (8) was slightly modified for its use to introduce microdamage into GaAs surfaces. The brittle nature of GaAs and the irregular sizes and shapes of GaAs wafers require certain process and equipment changes. Such changes are described in the Appendix II(a,b). In this study, ISS damage is applied to the backside of GaAs wafers with 6 to 12.5 watts of power at a resonance frequency of 1.5 kHz for 1.5 to 3.5 minutes.

The influence of ISS gettering on epitaxial layer quality is studied using liquid phase epitaxial layers grown on the front surface of ISS'ed wafers at 850°C in a H₂ ambient using an experimental procedure described in Ref. (10). The epitaxial layers are approximately 5 μm thick and are Ge doped to a concentration of 10¹⁸ atoms/cm³. The growth rate of the layer is about 6 μm/hr. During the epitaxial growth, the wafers experience an anneal period of 50 min. at the growth temperature. After the growth, the wafer backsides have shiny surfaces without apparent thermal degradation.

The defect studies are done by transmission electron microscopy (TEM). Samples for the TEM investigations are prepared by jet-etching with a solution of 3% Br₂ in methanol. Subsequently, samples are investigated in a Hitachi TEM operated at 200 keV.

RESULTS

Damage in GaAs: As-Stressed

Impact Sound Stressing (ISS) generates two modes of damage in GaAs wafer surfaces. One is a compressive mode and the other is an abrasive mode. In the compressive mode, the damage is created by the impact force of the tungsten balls hitting the surface nearly perpendicular. In the abrasive mode, the damage is generated by the impact force of balls hitting the surface at a shallow angle. The compressive and abrasive damage have been studied in detail. The results are as follows:

Compressive Damage

On (001) surfaces, the compressive mode generates damage sites roughly of square shape as shown in the insert of Fig. 1a. After preferential etching a dense network of defects is revealed. This network consists of one group of defects clustering around a damage center and another group that radiates from the center and propagates in <110> directions. Similar characteristics are observed for wafers of (111) surface orientation, Fig. 1b.

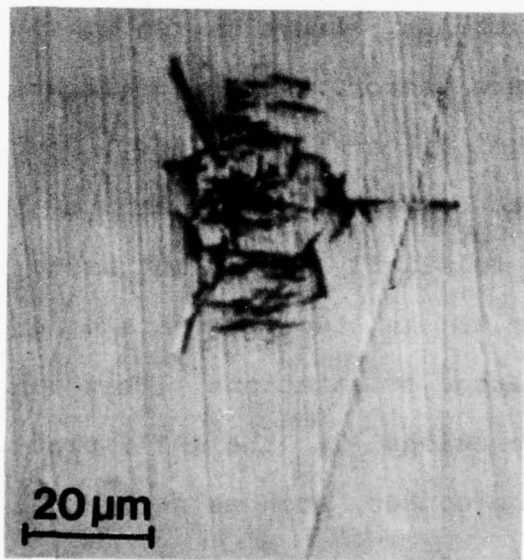
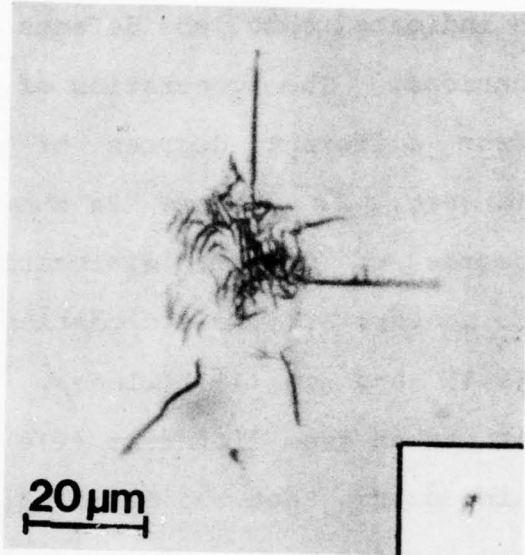


Fig. 1 Optical micrographs showing the compressive mode of ISS damage in (a) (001) and (b) (111) wafer surfaces.

TEM investigations indicate that the defects revealed by etching are dislocations. The generation of dislocation arrays resulting from different degrees of compressive damage is shown in Fig. 2. Figure 2a shows that at a relatively low degree of damage, dislocation arrays emanate from a damage center, S. The dislocations propagate predominantly in (111) and in $(1\bar{1}1)$ planes. Analysis of dislocation contrast taken from different (110) , (400) and (113) reflections indicates that the dislocations in both planes have a common Burgers vector of $a/2[10\bar{1}]$. Thus the main characteristic of the compressive damage is the generation of dislocation arrays in two (111) slip planes with a common Burgers vector. As the dislocations move by conservative motion in a slip plane, one end of a dislocation tends to be pinned at the damage center, while the other end glides relatively easily and exits through the surface. This results in two segments of a dislocation lying in two different orientations. This can be clearly seen for the dislocations in the (111) plane. Segments pinned at the damage center, such as segment A, are in the $[1\bar{1}0]$ direction and make a 60° angle with its Burgers vector. The segments which exit through the surface, such as segment B, are nearly in screw orientation.

As the degree of damage increases, the dislocations so generated become denser and the distance of dislocation movement from the damage center increases as shown in Fig.

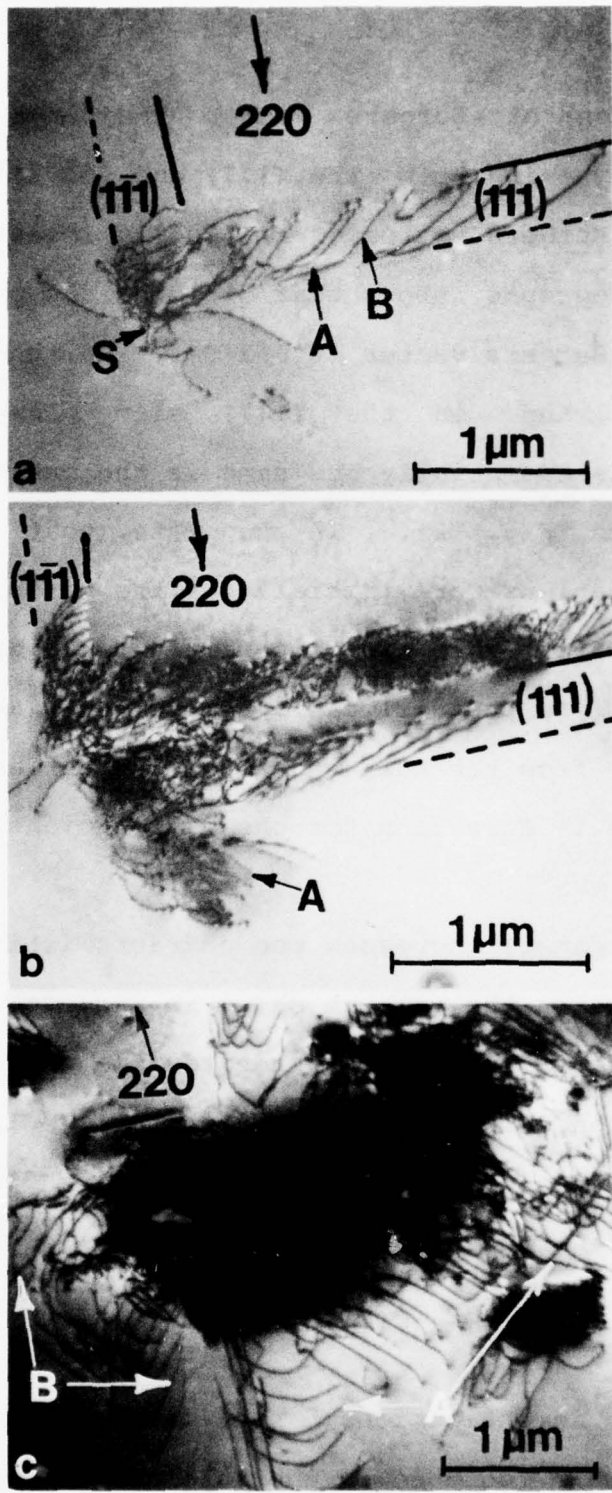


Fig. 2 Transmission electron micrographs showing the generation of dislocation arrays induced by the compressive ISS damage. The density of the dislocations generated increases as the degree of damage increases from (a) through (b) to (c).

2b. Determination of Burgers vector indicates that the dislocation arrays in both the (111) and the (1 $\bar{1}$ 1) plane have a common Burgers vector of $a/2[10\bar{1}]$. Investigations using stereomicrographs show that dislocations present in cluster A have a Burgers vector of $a/2[01\bar{1}]$ and tend to move in the (T11) and in the (1 $\bar{1}$ 1) slip plane. This characteristic is essentially the same as the one discussed in context with Fig. 2a. It suggests that the ISS generated dislocations are initially of the screw type and subsequently propagate into two slip planes containing their Burgers vectors. As the dislocations move, they experience more resistance from the bulk than from the surface. This leads to a change in direction for the dislocations.

As the amount of damage increases the characteristics of the dislocations remain the same as shown in Fig. 2c. For the case shown in Fig. 2c the damage generates two groups, A and B, of dislocation arrays: Group A dislocations lie in the (T11) and the (111) plane with $b = a/2[01\bar{1}]$, while group B dislocations lie in the (1 $\bar{1}$ 1) and in the (111) plane with $b = a/2[10\bar{1}]$.

During the TEM investigations, the dislocations near a damage center were found to be unstable and to move easily during electron beam exposure. A sequence of such a dislocation movement is shown in Fig. 3. The exposure time

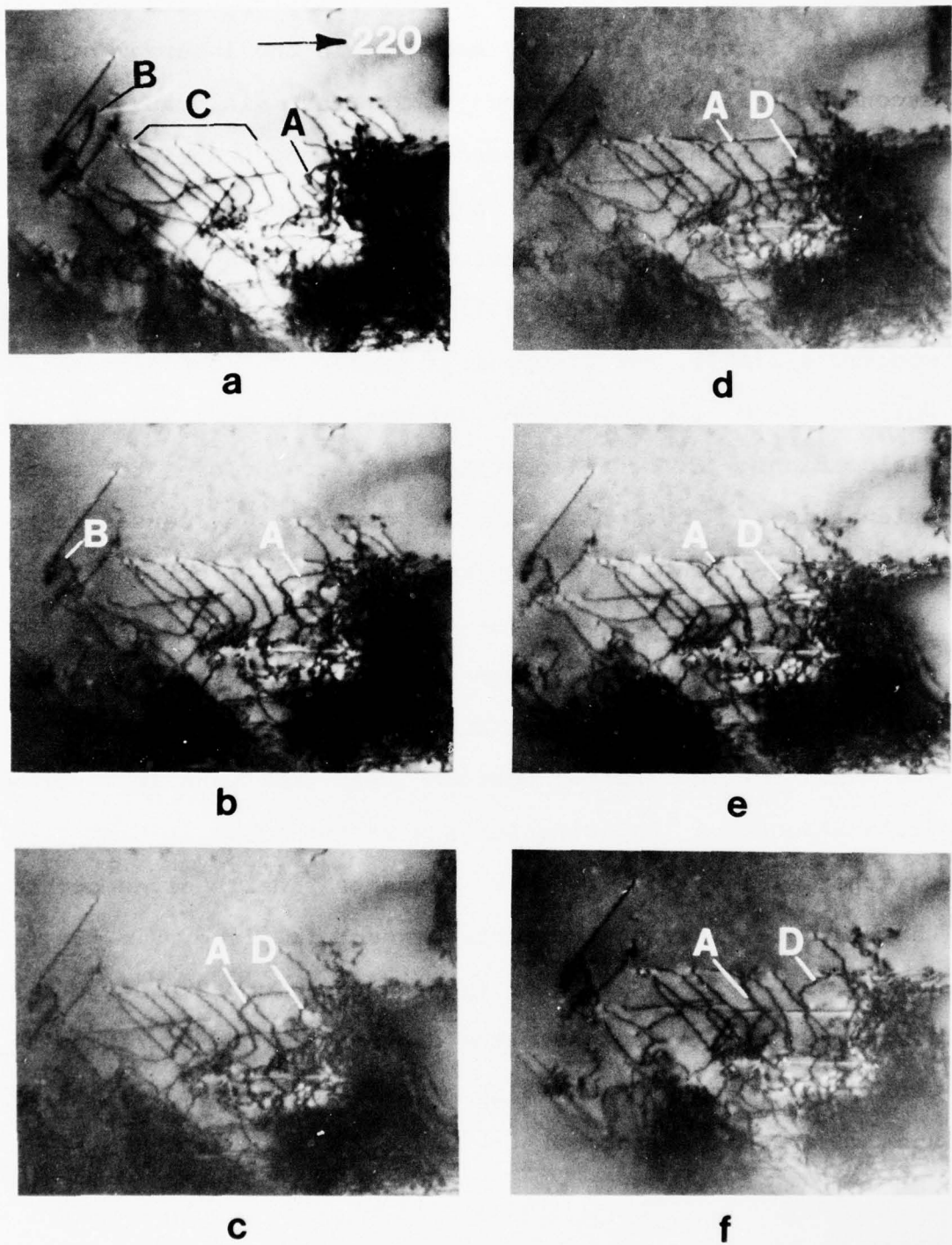


Fig. 3 Transmission electron micrographs showing dislocation movement during electron beam exposure. Dislocation loops A and D expand while B shrink. The interval of exposure time is about two seconds.

for the focused electron beam is in the interval of two seconds. Figure 3b shows that the dislocation loop designated A in Fig. 3a expands while loop B shrinks. Loop A continues to expand and loop B glides out to the surface in Fig. 3c. It should be noted that loop A and dislocation arrays C lying in the $(1\bar{1}1)$ plane have the same Burgers vector, $a/2[10\bar{1}]$, but of opposite sense. The opposite sense follows from the opposite curvature between loop A and dislocations C. Dislocations C are close to screw orientation. Further expansion of loop A causes it to arrange itself into three segments in $\langle 110 \rangle$ directions, Fig. 3c. One segment is in screw orientation and the other two make an angle of 60° with the Burgers vector. Once the screw segment moves close enough to one dislocation in C, the attraction force between the two parallel screw dislocations of opposite Burgers vector tends to bind them together, Fig. 3d. The 60° segments finally glide out to the surface leaving the screw segment in place, Fig. 3e,f. It can also be seen in these figures that loop D undergoes a similar expansion process. The dislocation configuration of dislocation arrays A and B in Fig. 2c are best described by such an expansion process.

Abrasive Damage

Abrasive damage is observed less frequently. It appears as long fine scratches, Fig. 4a. TEM investigation shows that

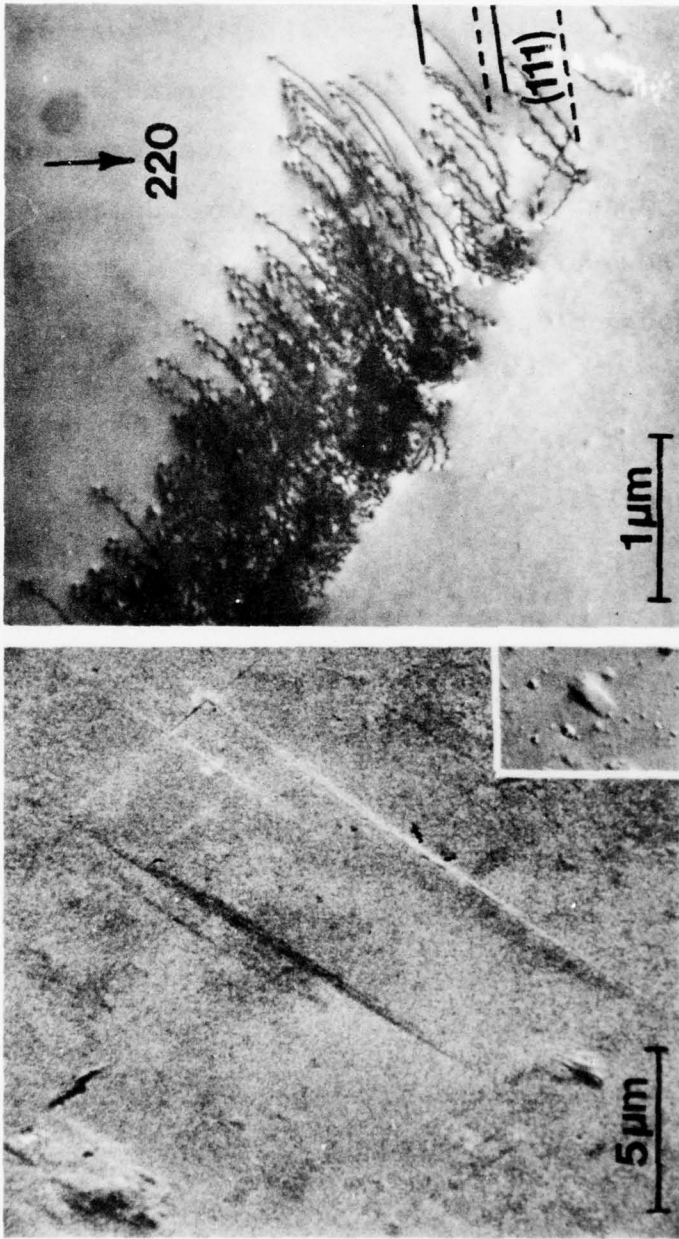


Fig. 4 (a) Scanning electron micrograph showing the abrasive ISS damage which appears as long fine scratches on the wafer surfaces.

(b) Transmission electron micrograph showing that the abrasive damage generates a group of dislocations in parallel (111) planes.

this mode of damage essentially generates a group of dislocations in parallel (111) planes, Fig. 4b. The Burgers vector of these dislocations is $a/2[10\bar{1}]$. Most of the dislocations are close to screw orientation. The characteristics of these dislocations are essentially similar to those generated by compressive damage. The abrasive damage, however, tends to generate dislocations predominantly in groups of parallel (111) planes. This is shown in Fig. 4b.

Damage in GaAs: Annealed

Annealing of ISS damage at high temperatures causes substantial changes in damage characteristics. The changes involve transformation of dislocation arrays into dislocation networks, dislocation loops and stacking faults. The formation of dislocation networks is usually associated with the relief of stress in a damage center as shown in Fig. 5a. When the ISS damage is sufficiently high, the networks extend quite often to the vicinity of a damage center, Fig. 5b. Examination of stereomicrographs shows that the networks are three-dimensional and consist of dislocation segments approximately in $<110>$ directions. The segments are relatively long for those in the $<110>$ directions parallel to the (001) surface and relatively

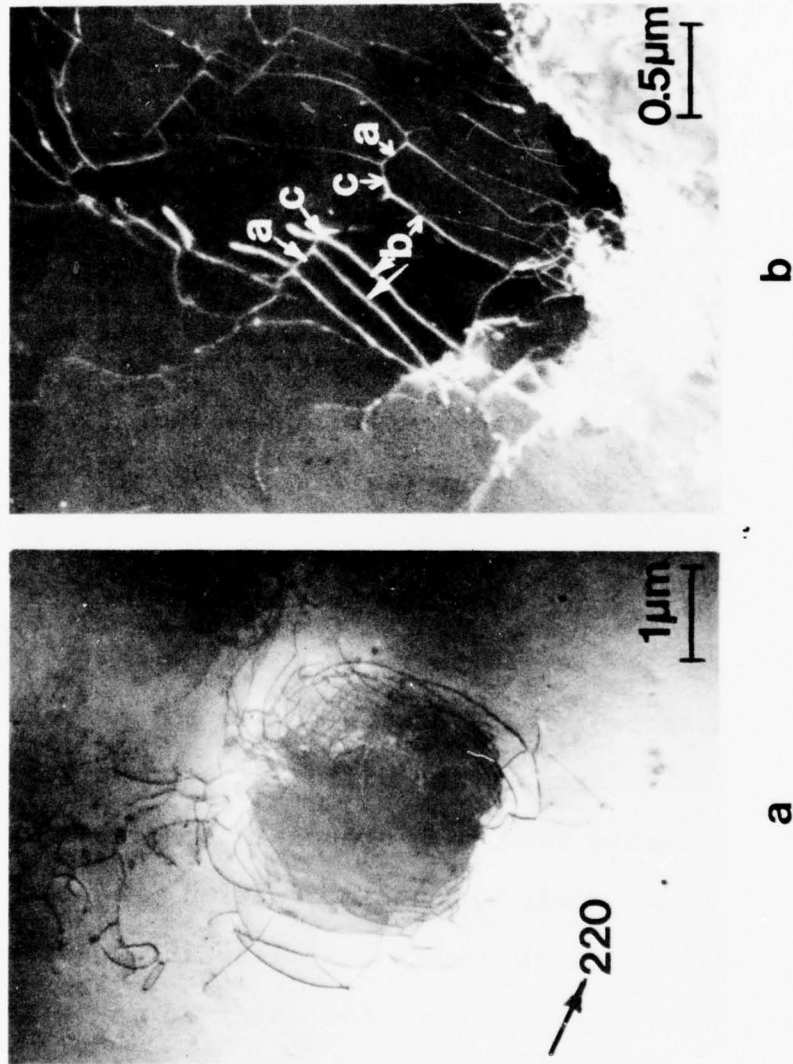


Fig. 5 Transmission electron micrographs showing that (a), annealing of ISS damage results in formation of dislocation networks in a damage center, and (b) the networks extend to the vicinity of a damage center when the ISS damage is sufficiently high.

short for those in the inclined <110> directions. It is evident in Fig. 5b that the intersection of two dislocations results in the formation of a triple node. Analysis of the Burgers vectors indicates that the Burgers vectors of the dislocations a , b and c is $b_a = a/2[\bar{1}10]$, $b_b = a/2[01\bar{1}]$ and $b_c = a/2[\bar{1}10]$, respectively. The corresponding dislocation directions are in the [1T0], [110] and [101] directions. Thus, they are all 60 degree dislocations.

The formation of such dislocation networks is a result of stress relaxation of ISS damage during annealing. As in the case of electron beam exposure, glide is the main mode of dislocation motion during annealing. As shown in Fig. 4, dislocation loops expand by glide and develop into 60° and screw segments. It is further shown in Fig. 5 that a relatively high degree of ISS damage tends to generate two groups of dislocation arrays with different Burgers vectors. When two 60° segments from such groups intersect, a triple node forms. The dislocation interaction reduces the dislocation energy by one-half. Similar arrangements of misfit dislocation networks have been observed in epitaxial layers of $\text{GaAs}_{1-x}\text{P}_x$ grown on GaAs substrates (11). Mader and Blakeslee (11) discussed the formation mechanism of such dislocation networks in detail.

Annealing also induces formation of stacking faults. In

general, the formation of these faults is due either to stress relief of ISS damage or due to the dissociation of dislocations. A fault generated by stress relief is shown in Figs. 6. Figure 6a is taken with the diffraction condition such that the fault is out of contrast. The Moire fringes shown are very complicated near the damage center and become regular arrays at the tip of the fault. Figure 6b shows that, at the tip, the fringe contrast associated with the fault changes in a sequence of three neighboring segments. The change in fault contrast arises from the change in fault nature. The nature of three neighboring segments changes from intrinsic, extrinsic to non-faulting segments. Such a fault can be considered to consist of layers of overlapping twins. The intrinsic segments are one-layer twins, and the extrinsic segments are two-layer twins. The non-faulting segments are three-layer twins. The fringe contrast arising from a three-layer twin is relatively weak. It becomes evident that relaxation of ISS damage stresses during annealing proceeds by shearing and rearranging of bonds between neighboring (111) planes. The onset of this process is the generation of overlapping twins. Similar overlapping twins have been observed in deformed silicon (12) and electron-beam heated Ge (13).

Stacking faults generated by dissociation of screw dislocations are shown in Fig. 7a. It can be seen that

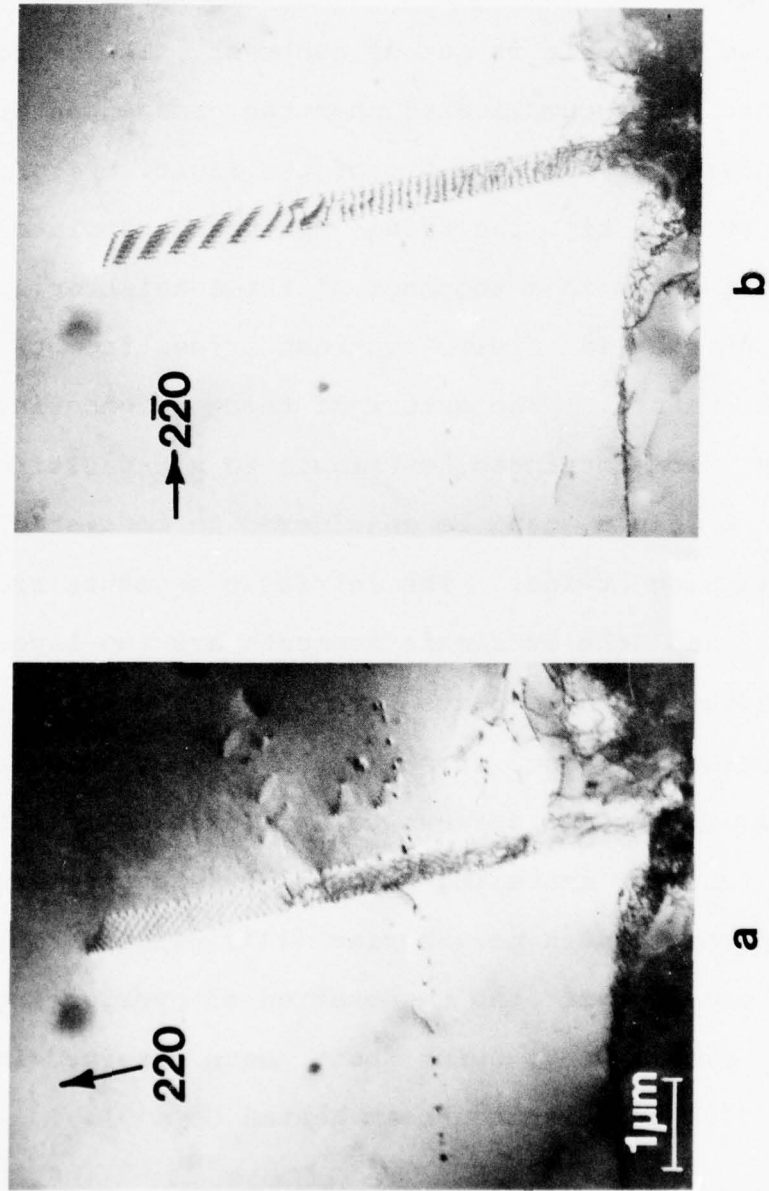


Fig. 6 Transmission electron micrographs showing the formation of stacking faults due to stress relief of ISS damage during annealing. (a) (220) and (b) ($2\bar{2}0$) reflections.

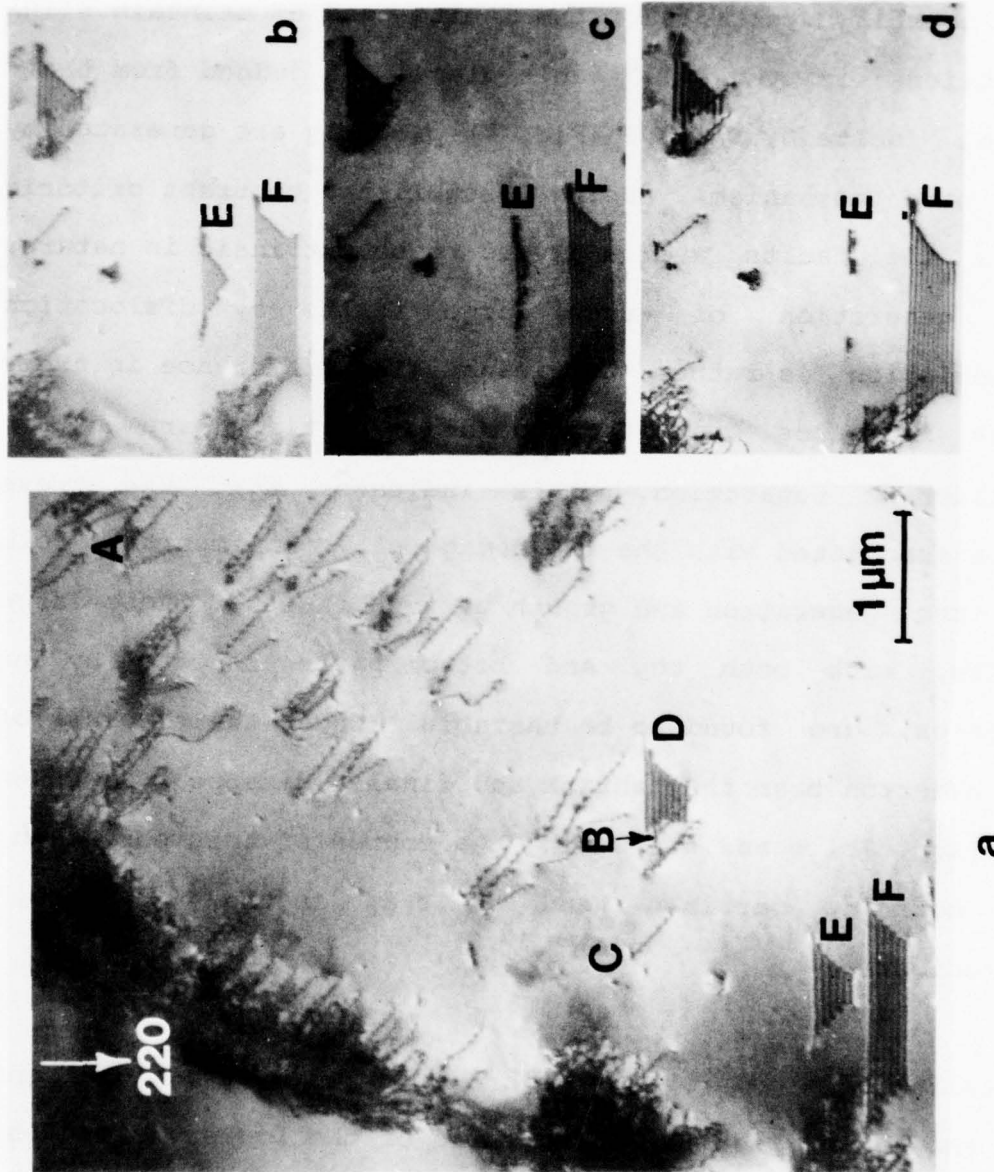
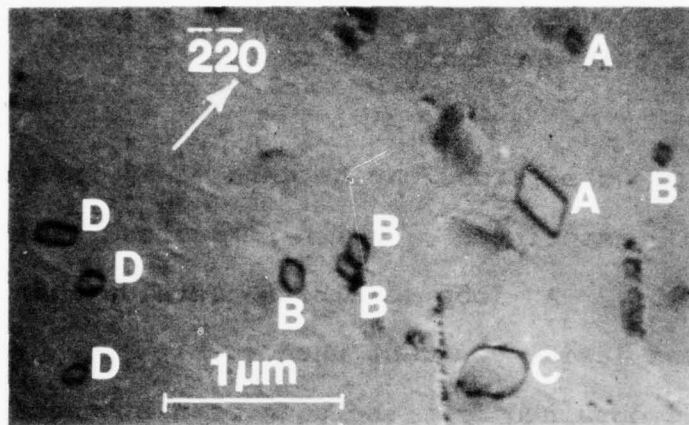


Fig. 7 Transmission electron micrographs showing (a), stacking faults generated by dissociation of screw dislocations in positions A, B, and C. (b), (c) and (d) shows that faults D, E, and F shrink under the exposure of electron beam.

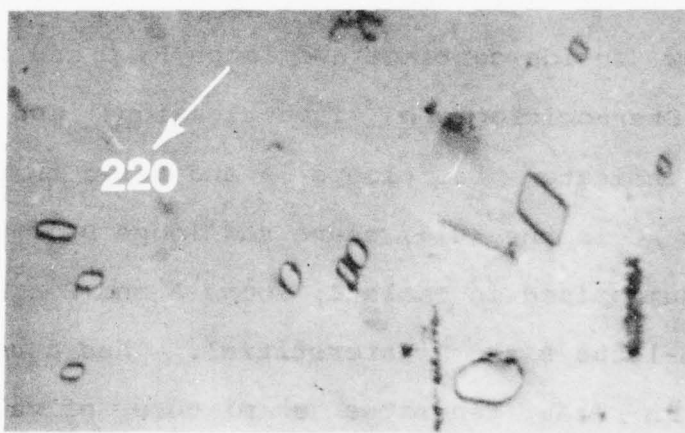
dissociation of the dislocations results in formation of stacking faults near the wafer surface in positions A, B and C.

The bounding partials of the faults tend to maintain <110> directions in the (111) fault plane. As judged from their shape, faults D, E and F (Fig. 7) probably are generated by the same mechanism. Using established contrast criteria (14), the faults are analyzed to be extrinsic in nature. The generation of such large faults by dislocation dissociation is rather surprising. The difference in their sizes indicates that the bounding partials are not in equilibrium separation. This indicates that the stress field associated with the ISS damage plays an important role for the generation and growth of such faults. These large faults, with both top and bottom parts truncated by the surfaces, are found to be unstable. Under the exposure of the electron beam they shrink and finally disappear as shown in Figs. 7b, c and d. During the course of this shrinkage, the bounding partials tend to stay in the <110> growth directions.

Annealing also generates a high density of dislocation loops as shown in Figs. 8. The size of the loops varies from several hundred to several thousand Angstroms. These loops lie in {110} planes. The Burgers vectors, b , of the loops



a



b

Fig. 8 Transmission electron micrographs showing that annealing of ISS damage also generates a high density of dislocation loops.
(a) (220) and (b) (220) reflections.

are identified as $(a/2) <110>$ normal to the loop plane. In most cases, these prismatic loops are inclined to the (001) surface rather than perpendicular to it.

The nature of the loops can be determined from the image displacement associated with reversed diffraction conditions (15). A loop exhibits outside contrast when $(g \cdot b)_s > 0$ and inside contrast when $(g \cdot b)_s < 0$. The nature of a loop is obtained from the sign of $n \cdot b$, where n is the loop plane normal. A loop is "interstitial" for $n \cdot b > 0$ or is "vacancy" for $n \cdot b < 0$. In comparing Fig. 8b with Fig. 8a loops A show inside contrast and loops B, C and D outside contrast. Stereomicrograph investigations and tilting experiments indicate that loops A and B lie in the $(\bar{1}01)$ plane, loops C in the (011) plane and loops D in the $(0\bar{1}1)$ plane. As summarized in Table I, loops A and C are vacancy in nature and loops B and D interstitial. Thus annealing of ISS damage in GaAs generates a mixture of vacancy and interstitial loops.

The depth of ISS damage after annealing is also determined. After removal of a $15 \mu m$ surface layer, no defects associated with residual damage are observed. Therefore, it is estimated that the ISS damage is confined to a surface layer less than $15 \mu m$ in depth. For further details on damage depth see Appendix II(b).

TABLE I. Determination of the Nature of Dislocation Loops

Fig. 8a, $g = \overline{2}\overline{2}0$, $s > 0$							
Loop	Loop plane	Contrast	$(g \cdot b)_s$	$g \cdot b$	$g \cdot n$	$n \cdot b$	Loop nature
A	($\overline{1}01$)	Inside	< 0	< 0	> 0	< 0	Vacancy
B	($\overline{1}01$)	Outside	> 0	> 0	> 0	> 0	Interstitial
C	(011)	Outside	> 0	> 0	< 0	< 0	Vacancy
D	(0 $\overline{1}1$)	Outside	> 0	> 0	< 0	> 0	Interstitial

For control measurements annealed wafers without ISS damage were also studied. Investigation of such wafer backsides revealed a high density of square or rectangular etch pits. These etch pits always contained some residual precipitates, and are shown in Fig. 9a. It is assumed that the formation of the etch pits is the result of contamination during the annealing process. When the precipitates are sufficiently large, dislocations are generated around the precipitate sites, Fig. 9b. Contrary to the ISS damaged surfaces, no dislocation loops are observed in the annealed non-damaged surfaces. This control measurement confirms that the formation of dislocation loops in ISS damaged surfaces is related to the stresses generated by the ISS damage.

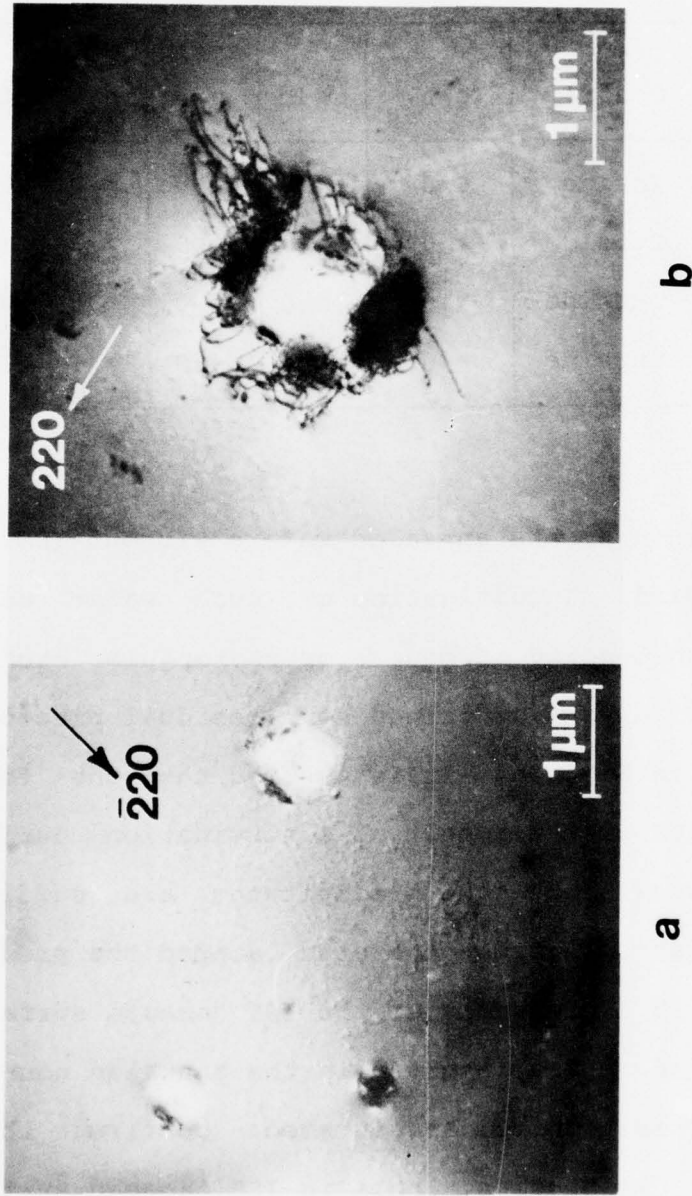
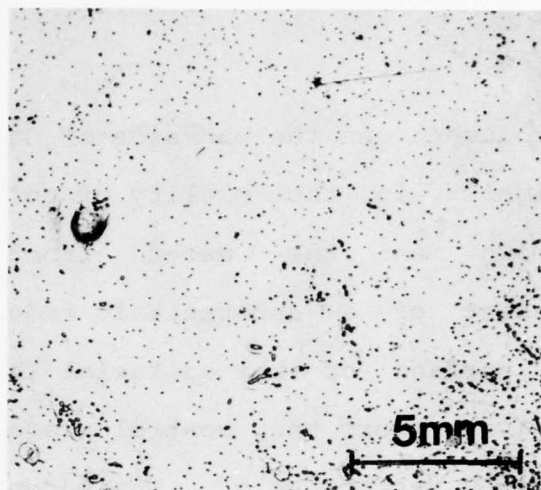


Fig. 9 Transmission electron micrographs showing (a) residual precipitates and (b) dislocations generated due to the relief of the stress set up by the precipitates in the backsides of annealed wafers without ISS damage.

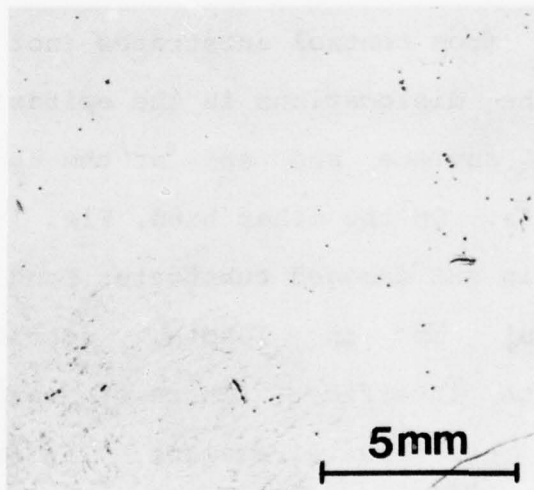
The Influence of ISS Damaged Substrates on Epitaxial Quality

ISS damage introduced on the backside of GaAs substrates produces improvements in the quality of epitaxial layers subsequently grown on the wafer front side. The improvements consist of a substantial reduction in pit density at the surface of the epitaxial layer. This is shown in Figs. 10a,b for the control wafer and the ISS damaged substrates, respectively. The second improvement results in a confinement of the "threading" dislocations to the epitaxial-substrate interface. Transmission x-ray topographs taken from control substrates (not ISS'ed) show that most of the dislocations in the epitaxial layer are inclined to the surface and end at the epitaxial layer surface, Fig. 11a. On the other hand, Fig. 11b shows that the dislocations in ISS damaged substrates tend to have long segments, several mm in length, confined at the epitaxial-substrate interface. These segments are seen to align almost in the $<110>$ directions. The confinement of long dislocation segments at the epitaxial-substrate interface causes the dislocations to make a shallower angle to the epitaxial layer surface.

To obtain additional clarifications and because of the relatively low resolution of x-ray topographs, the



a



b

Fig. 10 Optical micrographs showing the pit density at the epitaxial surface for (a) the control wafer, and (b) the ISS damaged wafer.

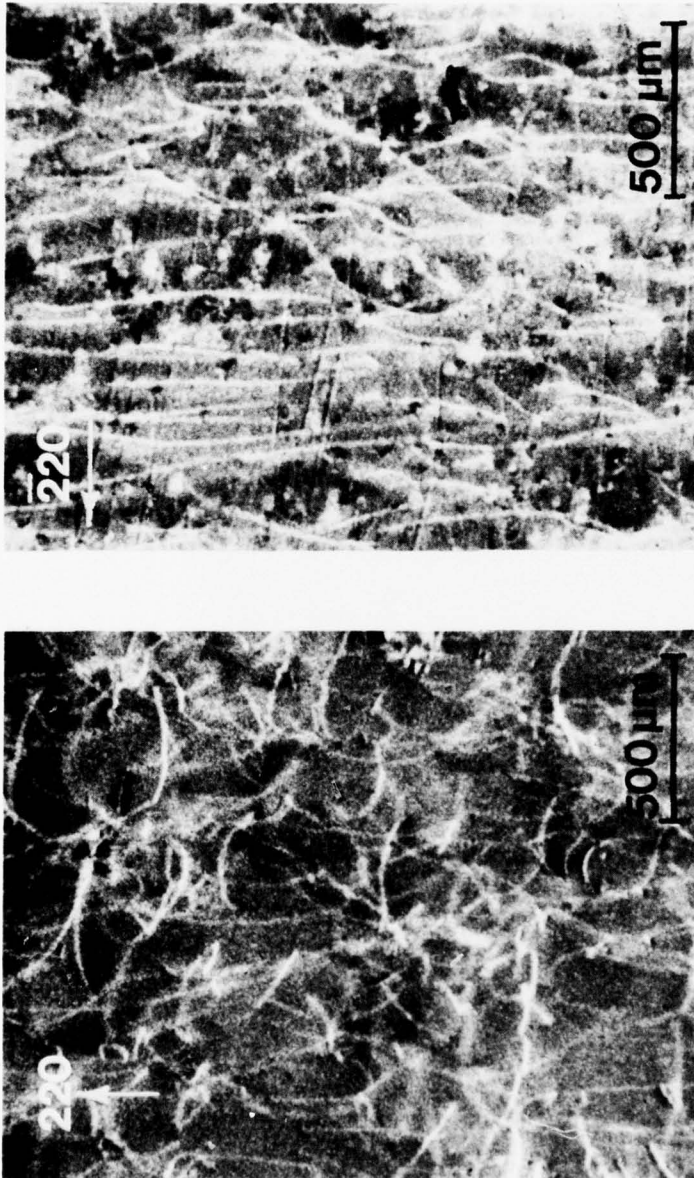


Fig. 11 Transmission X-ray topographs showing (a) most of the dislocations in the epitaxial layer of control substrates are inclined to the surface, and (b) the dislocations in ISS damaged substrates tend to be confined at the epitaxial-substrate interface.

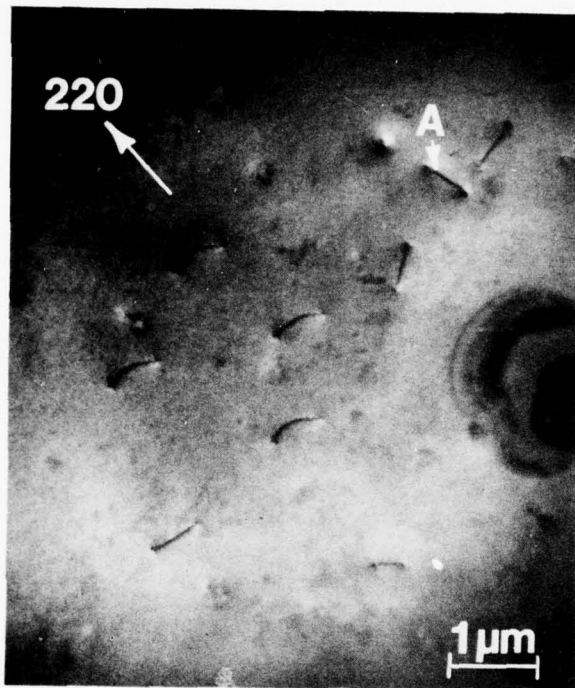


Fig. 12 Transmission electron micrograph showing that the dislocation density in the epitaxial layer of the control substrates is as high as 10^6 to 10^7 per cm^2 .

samples were further investigated through transmission electron microscopy. In the control substrates, the epitaxial layer surface has a high density of dislocations in the range of 10^6 and 10^7 per cm^2 , (Fig. 12). The dislocations are inclined to the surface and are almost in a $\langle 110 \rangle$ direction making an angle of 60° with their Burgers vectors. Most of the dislocations have their Burgers vector also inclined to the surface. In Fig. 12, only dislocation A has a Burgers vector parallel to the surface. Investigations of the epitaxial layer surface on ISS damaged substrates shows a much lower dislocation density in the epitaxial surface. In such epitaxial layers dislocations are rarely observed. If they are present, they make a relatively shallow angle with the epitaxial layer surface. These TEM results are in good agreement with x-ray topographic observations and confirm that ISS can be gainfully employed to produce epitaxial GaAs layers of superior quality.

DISCUSSION

Impact Sound Stressing of semiconductor wafer surfaces is obviously an elegant technique to introduce mechanical damage into wafer surfaces in a controlled manner. Thus it becomes possible to study damage in wafer surfaces and its consequences on crystal quality during semiconductor processing. For the following it is useful to

compare differences in the characteristics of ISS damage obtained in GaAs and in Si. Details of ISS damage in silicon were previously reported (2). For comparison the differences in damage characteristics between Si and GaAs are summarized in Table II.

TABLE II. Characteristics of ISS Damage in Si and GaAs

ISS conditions		Mechanical Damage Characteristics of Covalent Crystals	
		Si*	GaAs
As damaged	Compress- ive	Brittle fracture with cleavage dislocations confined in cleavage planes	Plastic deformation with dislocation arrays gliding in (111) planes
	Abrasive mode	Plastic defor- mation with gener- ation of shear loops up to 0.3 μm in size	Plastic deformation with dislocation arrays gliding in (111) planes
After annealing at $T \approx 0.75 T_m$ **		Generation of dislocations in N_2 ambient. Gener- ation of stacking faults in oxidiz- ing ambient	Cross-linked dislo- cation networks, stacking faults dislocation loops
*For details see ref. (2) ** T_m = melting temperature in absolute scale			

The compressive mode of ISS damage usually results in cone fracture on a wafer surface. A cone fracture causes three different types of lattice distortion, namely lattice rotation, bending and translation of both parts of the fractured surface. In general all three effects are present simultaneously. In silicon at room temperature, the compressive damage causes brittle fracture (2). The stresses around the tip of fracture cracks are not plastically relieved through dislocation generation. In GaAs plastic deformation occurs at room temperature. This leads, in GaAs, to the generation of dislocation arrays which are predominantly screw type in character. These dislocations lie in two (111) planes which both contain the Burgers vector of the screw dislocations. As a result of stress relief in GaAs dislocation movement, up to several micrometers, proceeds by glide. Abrasive damage in GaAs essentially induces the same dislocation arrays lying in parallel (111) planes. In contrast abrasive damage in silicon causes generation of microsplits (2). The microsplits have been shown to be composed of pile-ups of shear dislocation loops of up to $0.3 \mu\text{m}$ in size (2). The generation of such shear loops indicates that some plastic deformation occurs also in silicon damaged by the abrasive mode. The relative difficulty for dislocation generation and dislocation movement in silicon arises from the

relatively high dislocation energy. For silicon, the dislocation energy is 6.2 eV for screw dislocations and 7.9 eV for 60° dislocations (16). For GaAs, the corresponding values are 3.9 and 5.4 eV (16).

After annealing at a temperature of 1000°C for silicon and of 850°C for GaAs, which corresponds to approximately 75% of the melting temperature in the absolute scale, these two materials show significant differences in their annealed mechanical damage (ISS) characteristics. The damage characteristics in silicon are strongly influenced by the annealing ambient. In a N₂ ambient, annealing causes generation of dislocations. The dislocations move by glide. In an oxidizing ambient, the formation of Frank type stacking fault occurs. The growth of the faults occurs by climb.

In annealed GaAs dislocation motion is observed to proceed by glide as well as by climb. Thus the annealing of ISS damage in GaAs results in the formation of cross-linked dislocation networks, stacking faults and dislocation loops. The formation of dislocation networks and stacking faults is associated with the interaction and the dissociation of perfect dislocations by glide. The formation of prismatic dislocation loops occurs by climb.

The damage results observed for silicon (2) are in good agreement with those reported previously (17,18). At room temperature, silicon shows brittle fracture. Plastic flow arises as a result of the accommodation of the displacements due to block slip (17). At a deformation temperature ($T = 0.5$ to $0.8 T_m$), dislocation glide is dominant and cross slip is activated (18). At a deformation temperature ($T \geq 0.8 T_m$), gliding of dislocations combined with climb occurs (18).

For GaAs at room temperature, dislocation motion by glide is dominant. At a deformation temperature of $T = 0.75 T_m$ glide and climb mechanisms are operative. Intersection of glissile dislocations results in the formation of dislocation networks. Stress relaxation of ISS damage in GaAs during annealing proceeds by shearing and rearrangement of the bonds between neighboring (111) planes. The onset of this process is the generation of stacking faults consisting of overlapping twins. Similar faults have been observed previously in deformed silicon (12) and in Ge locally heated by electron beams (13).

Stacking faults can also be generated by dissociation of screw dislocations. Such a dissociation is in good agreement with Holt's model (19). Holt (19) proposes that

in zinc-blend materials, only the screw dislocation is able to rearrange its core bonds without forming wrong bonds. Thus bond rearrangement will occur most effectively along the screw oriented portion of a dislocation leading to elongation of the lattice parallel to the Burgers vector of the screw dislocations. This model can be used to explain the screw configuration of dislocation arrays generated by ISS damage at room temperature.

Formation of prismatic loops in GaAs is a subject of controversy. Such dislocation loops have been observed in annealed GaAs heavily doped with tellurium (20,21), selenium (21), or silicon (22), and during degradation of $\text{Ga}_{1-x}\text{Al}_x\text{As}/\text{GaAs}$ during laser action (23). Narayaman and Kachare (22) observed the presence of loops only in heavily doped Si GaAs ($\sim 4 \times 10^{19} \text{ Si/cm}^3$). Lightly doped Si ($\sim 1 \times 10^{18} \text{ Si/cm}^3$) and undoped GaAs crystals did not contain any prismatic dislocation loops after annealing.

The dopant concentration used in our investigation is about $6.5 \times 10^{17} \text{ Sn/cm}^3$. Note that in our investigation dislocation loops are not observed in the non-damaged GaAs surfaces after annealing. However, they are observed in ISS damaged surfaces. This would indicate that the formation of prismatic dislocation loops in GaAs is related to stresses, such as are set up by dopants, ISS stress centers, and the

one present at epitaxial interfaces.

The exact mechanism for the generation of prismatic dislocation loops in GaAs is still a subject of some controversy (20-23). In tellurium doped GaAs, the loops were determined to be of the vacancy type by Laister and Jenkins (20). However, Hutchinson and Dobson (21) found them to be interstitial. In silicon doped GaAs, the loops were found to be vacancy in nature (22). In ISS damaged, Sn doped GaAs surfaces, we observe a mixture of vacancy and interstitial loops. Similar to our results are the observations of interstitial dislocations dipoles and vacancy loops in $\text{Ga}_{1-x}\text{Al}_x\text{As}/\text{GaAs}$ lasers reported recently (23).

A model advanced by Petroff and Kimerling (23) proposes a dislocation climb mechanism for compound semiconductors of the zinc blend structure. In this model a supersaturation of only one type of point defects is required for dislocation climb and a trail of point defects of the opposite type is left behind the climbing dislocation. Condensation of both types of point defects may result in both types of dislocation loops as observed in the our investigation.

ISS damage of the backside wafer surface does not only cause the generation of dislocation loops by absorption of point defects, but also reduces the density of threading dislocations in the epitaxial surface. Matthews and Blakeslee (24) described several techniques to enhance crystal perfection in epitaxial layers. Accordingly, the density of threading dislocations can be reduced by the use of misfit stresses which bend the dislocations over into the interfacial plane. Experimental evidence to support this mechanism has been reported (25,26). Olsen, et al (26) demonstrated that this mechanism works only for epitaxial layers which are in compression but not for those which are in tension. ISS damage undoubtedly puts the damaged back surface into tension and thus the epitaxial layer into compression. Ion implantation damage gettering relies on the same phenomenon.

The use of ISS damage to reduce threading dislocations and to confine them at the epitaxial-substrate interface is therefore in principle similar to the technique used by Olsen, et al (26). It also indicates and confirms the importance of surface stresses in semiconductor wafers as a means to engineer defect low or defect free wafer surfaces. The sign of the surface stress state of a wafer surface (tensile back; compressive front) controls the gettering

action in a semiconductor wafer during high temperature processing.

SUMMARY

The principle of defect engineering is applied to GaAs substrates to produce epitaxial layers of low crystallographic defect density. Defect engineering is achieved through control of surface stresses in GaAs wafers during high temperature processing. Surface stress control is obtained through Impact Sound Stressing damage introduced on wafer backsides before epitaxial processing. Thus, epitaxial GaAs layers obtained through liquid phase epitaxy contain low dislocation numbers through confinement of threading dislocations to the epitaxial-substrate interface.

A detailed analysis of ISS damage in GaAs before and after annealing is given.

The characteristics of ISS damage in GaAs are investigated through transmission electron microscopy. It is found that ISS generates two modes of damage. One is compressive and the other one is abrasive. At room temperature, both damage modes cause plastic deformation in GaAs. This results in the generation of dislocation arrays. Such dislocation arrays are predominantly of the screw type, emanate from a

damage center, and glide in (111) planes.

After annealing at 850°C, stress relief of ISS damage results in the formation of cross-linked dislocation networks, stacking faults, and dislocation loops. During annealing dislocation motion proceeds by glide and climb. The formation of dislocation networks arises from the intersection of glissile dislocations with different Burgers vectors. Stress relaxation of ISS damage through shearing and rearrangement of bonds between neighboring (111) planes generates stacking faults consisting of overlapping twins. Stacking faults formed by the dissociation of screw dislocations are also observed. The formation of prismatic dislocation loops is observed and shown to occur by climb. These loops are either of the vacancy or of the interstitial type. Their formation is related to the stresses induced by the ISS damage.

ACKNOWLEDGMENTS

LPE growth was provided by M. Small and R. Potensky of IBM Research Laboratories, Yorktown Heights. Technical support was given by: H. Ilker, transmission electron microscopy and C. Hoogendoorn, X-ray topography.

REFERENCES

1. G. H. Schwuttke, Technical Report No. 3, Contract No. DAHC-15-72-C-0274, (Jan. 1974).
2. G. H. Schwuttke, ARPA Contract No. DAHC-15-72-C-0274, Technical Report No. 7, (Jan. 1976).
3. E. J. Mets, J. Electrochem. Soc., 4, 420 (1965).
4. J. E. Lawrence, Met. Soc. AIME, 242, 484 (1968).
5. T. E. Seidel and R. L. Meek, in Proceedings of the 3rd International Conf. on Ion Implantation in Semiconductors, edited by B. L. Crowder, p. 305, Plenum, New York (1973).
6. C. M. Hsieh, J. R. Mathews, and H. D. Seidel, Appl. Phys. Lett. 22, 238 (1973).
7. C. O. Bozler, J. P. Donnelly, W. T. Lindley and R. A. Reynolds, Appl. Phys. Lett., 29, 698 (1976).
8. G. H. Schwuttke, ARPA Contract No. DAHC-15-72-C-0274, Technical Report No. 4, (July, 1974).

9. G. H. Schwuttke, RADC-TR-76-256, (Sept. 1976).
10. L. R. Dawson, J. Cryst. Growth, 27, 86 (1974).
11. S. Mader and A. E. Blakeslee, IBM J. Res. Develop., 151, (March, 1975).
12. V. G. Eremenko and V. I. Nikitenko, phys. stat. sol., (a), 14, 317 (1972).
13. R. Meingast and H. Alexander, phys. stat. sol., (a), 17, 229 (1973).
14. R. Gevers, A. Art and S. Amelinckx, phys. stat. sol., 31, 563 (1963).
15. P. B. Hirsch, A. Howie, R. B. Nicholson, D. W. Pashley, and M. J. Whelan, "Electron Microscopy of Thin Crystals," p. 265, Plenum Pub. Co., New York, (1965).
16. H. Alexander and P. Haasen, phys. stat. sol., 22, 271 (1968).
17. M. J. Hill and D. J. Rowcliffe, J. Mat'l. Sci., 9, 1569 (1974).

18. A. L. Aseev, Yu. N. Golobokov and S. I. Stenin, phys. stat. sol., 28, 355 (1975).
19. D. B. Holt, J. Phys. Chem. Solids., 23, 1353 (1962).
20. D. Laister, and G. M. Jenkins, Phil. Mag., 23, 1077 (1971).
21. P. W. Hutchinson and P. S. Dobson, Phil. Mag., 30, 65 (1974).
22. G. H. Narayanan and A. H. Kachare, phys. stat. sol., 26, 657 (1974).
23. P. M. Petroff and L. C. Kimerling, Appl. Phys. Lett., 29, 461 (1976).
24. J. W. Matthews and A. E. Blakeslee, J. Cryst. Growth, 32, 265 (1976).
25. G. A. Rozgonyi, P.M. Petroff and M. B. Panish, Appl. Phys. Lett., 24, 251 (1974).
26. G. H. Olsen, M. S. Abrahams, C. J. Buiocchi and T. J. Zamerowski, J. Appl. Phys., 46, 1643 (1975).

Chapter 2

DIRECT IDENTIFICATION OF OXIDE PRECIPITATES IN ANNEALED SILICON CRYSTALS

by K. H. Yang, R. Anderson, H. F. Kappert and G. H. Schwuttke

INTRODUCTION

Prolonged annealing of Czochralski grown silicon crystals containing an oxygen concentration of about 10^{18} atoms/cm³ usually causes formation of precipitates (1-3). These precipitates are in general assumed to be a form of silicon oxide. This assumption is based on the fact that the oxygen concentration as measured by the IR spectroscopy is reduced after annealing. A study of the growth kinetics of the precipitates also strongly suggests that the precipitates are most likely silicon oxide (3). However, no direct evidence of the precipitates as a form of silicon oxide has been reported. The main difficulty arises from the fact that micro-analysis of the precipitates requires an instrument of both high spatial resolution and high detection sensitivity. Techniques such as electron diffraction fail to reveal extra dots or rings from the

precipitates (1-3). In this chapter, we report measurements of electron energy loss spectra obtained from such precipitates. Analysis of the spectra confirms that the precipitates are a form of silicon oxide.

EXPERIMENTAL

For this investigation, Czochralski grown silicon crystals with an oxygen concentration of about 10^{18} atoms/cm³ are used. The crystals are of <100> orientation and are doped with boron to a resistivity of 2 Ω-cm. Crystal sections approximately 50 mm in length are cut from the crystals and are subsequently annealed in dry oxygen at 1100°C for 40 hours. After annealing the crystal sections are sliced in wafers. The specimens are prepared for TEM investigation by jet etching with an etchant of 9 parts concentrate HNO₃, and 1 part 49% HF. Precipitates formed in the crystal bulk during annealing are analyzed with an electron energy loss analyzer attached to a JEOL 100-C field-emission gun equipped microscope operating at 80 keV. The electron energy loss spectra so obtained are calibrated using the loss of silicon 2p electrons at 99.2 eV as a standard. Energy losses at other levels are calculated through the use of an Orthoplex Coordinate Sensor, Model E 241, Ladd Research Industries, Burlington, Vermont.

RESULTS AND DISCUSSION

The energy loss analysis is particularly useful for the detection of low atomic number elements. It is more sensitive than traditional techniques based on x-ray emission because the K-shell energy loss signal remains constant with decreasing atomic number, whereas the x-ray production efficiency decreases (4). The main problem encountered in the present investigation is the requirement of a sample thickness of 1000\AA or less. Precipitates in a TEM specimen of this thickness range are usually etched out, leaving their replicas at the original precipitation sites. Figure 1 shows the precipitates in a specimen of $2 - 3000\text{\AA}$ thickness. Precipitates 1 and 2 remain intact at their original precipitation sites. The dislocation loops and helixes punched out from the precipitates lie in $\{110\}$ planes inclined to the (001) surface. Those in $\{110\}$ planes perpendicular to the (001) surface are etched out. Precipitate 3 has been etched out and moved from A to B. Quite often, the etched out precipitates assume hexagonal shape as do the precipitates 4 and 5. This is because the precipitates induced by the annealing of bulk crystals are octahedral in shape. The faces of the octahedral precipitates are the matrix-precipitate interfaces and are parallel to the $\{111\}$ planes of the silicon matrix. Once

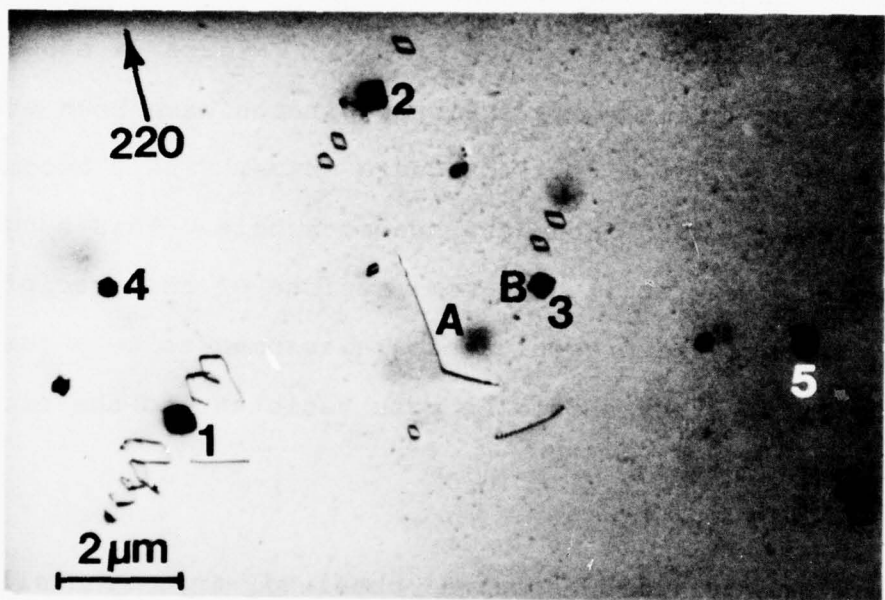


Fig. 1 Transmission electron micrograph showing precipitates and dislocation loops and helices in annealed bulk silicon crystals.

etched out, the precipitates tend to sit on the matrix surface with one of their octahedral faces. This results in a hexagonal projection of the precipitates.

The same etching characteristics persist for a specimen thickness decrease, to 1000\AA or less. Figure 2a shows two precipitation sites where the precipitates have been etched out. Site A has a regular square shape, Site B becomes a bump sticking out into the specimen hole. This suggests that Site B may still have some residue of the precipitate left. Because the precipitates are assumed to be a form of silicon oxide they should be more resistant to the etchant than silicon.

Electron energy loss spectra obtained from the silicon matrix and Site B (Fig. 2a) are shown in Figs. 3a and b, respectively. Both figures show the energy losses at 99 and 149 eV due to excitation of silicon 2p and 2s electrons, respectively, and the plasmon losses of silicon at 17 and 34 eV. The loss peaks between 99 and 149 eV result from the superposition of plasmon losses on the silicon 2p loss edge at 99 eV. One remarkable difference between these figures is that only Site B gives rise to energy loss at 532 eV. The loss at 532 eV is due to the excitation of oxygen 1s electrons. Energy filter images, Fig. 2b, taken at this

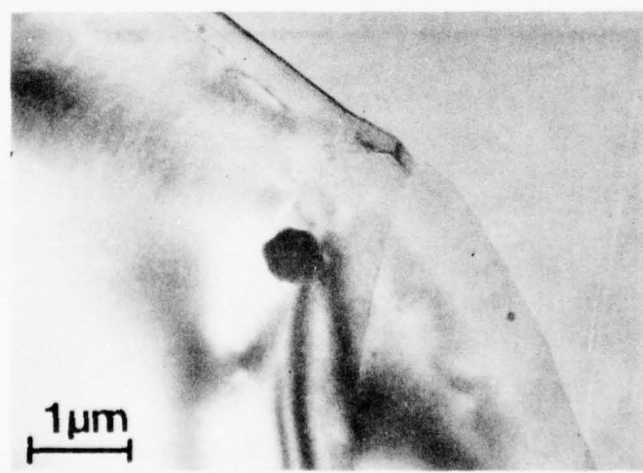
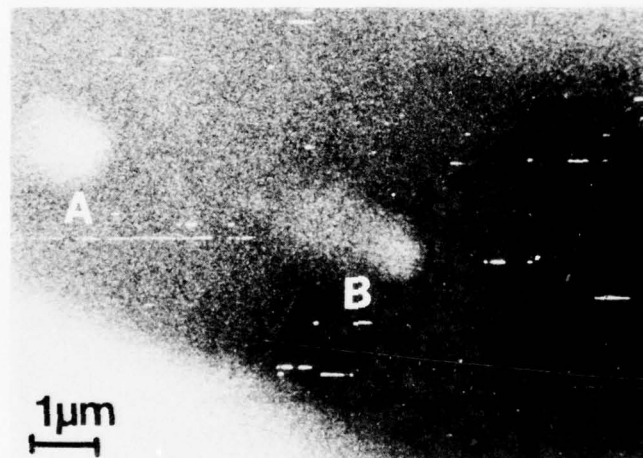
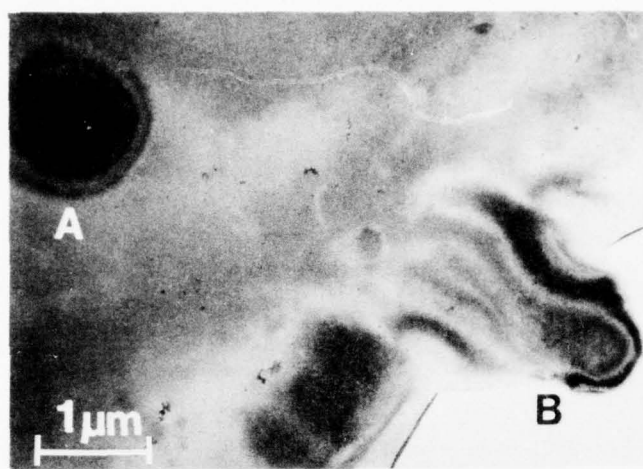


Fig. 2 Transmission electron micrographs showing (a), two precipitation sites, (b), energy filter image of (a) taken at the energy loss of 532 eV, and (c), a precipitate in a region less than 0.1 μm in thickness. Oxygen 45

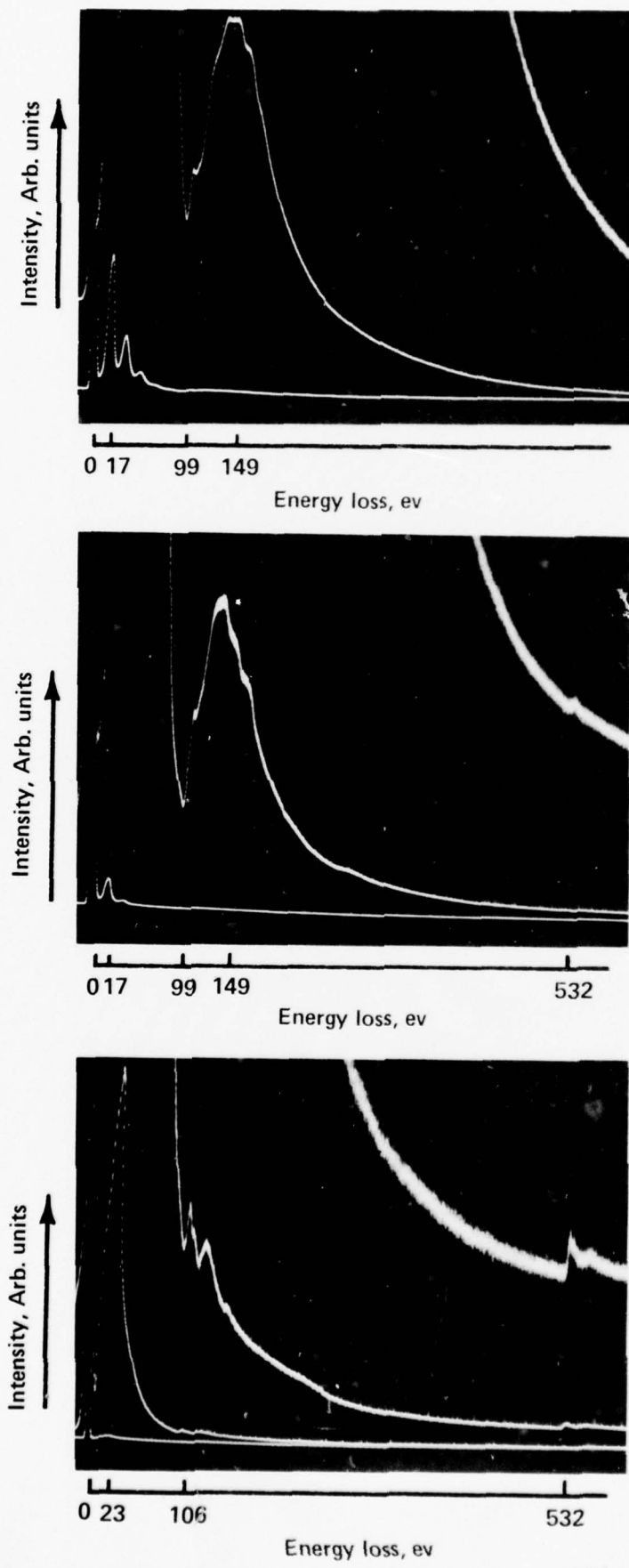


Fig. 3 Electron energy loss spectra of (a), the silicon matrix of Figs. 2(a&b) precipitation site B, and (c) thermally grown SiO_2 .

energy loss, show that the precipitate sites are brighter than the surrounding matrix, indicating residue of oxide precipitate left in such sites.

The energy loss at 532 eV is further checked through the spectra of thermal SiO_2 . The spectrum of a 500 \AA -thick SiO_2 , Fig. 3c, clearly reveals the energy loss of oxygen 1s excitation at 532 eV. In addition, the plasmon loss of SiO_2 at 23 eV and the superposition of the plasmon loss on the oxygen 1s loss edge can also be seen in this figure. The bonding environments of the Si in SiO_2 induces a shift in the Si 2p loss edge from 99 to 106 eV. The shift of Si 2p binding energy has been found to increase with the value of x in SiO_x (5).

Investigation of etched out precipitates such as the one shown in Fig. 2c show the same energy loss at 532 eV. Numerous spectra obtained from the precipitation sites and precipitates in this area essentially indicate the same results: the precipitates contain oxygen. The results of this investigation provide, for the first time, direct identification of the precipitates as a form of silicon oxide.

CONCLUSION

Electron energy loss spectra of precipitates formed in annealed silicon crystals are investigated. Precipitates as well as residue of precipitates in precipitation sites yield an energy loss spectrum at 532 eV. It is shown that this energy loss is due to the excitation of oxygen 1s electrons. Therefore the precipitates are silicon oxide.

REFERENCES

1. T. Y. Tan and W. K. Tice, Phil. Mag., 30, 015 (1976).
2. D. M. Maher, A. Standinger and J. R. Patel, J. Appl. Phys., 47, 3813 (1976).
3. G. H. Schwuttke and K. H. Yang, Technical Report No. 2, ARPA Contract No. N00173-76-C-0303, Sept. 1977.
4. R. F. Egerton, C. J. Rossouw and M. J. Whelan, "Developments in Electron Microscopy and Analysis", edited by J. A. Venables, P. 129, Academic Press, New York (1976).
5. S. I. Raider and R. Flitsh, J. Electrochem. Soc., 123, 1756 (1976).

APPENDIX I

Table of Contents of Reports Published

I. Contract No. DAHC-15-72-C-0274

Technical Report No. 1 - Table of Contents

Microsplits in Silicon Surfaces
and Their Influence on MOS Storage Time

1. Introduction

2 Experimental

3. Results of Structural Investigations

3.1 Transmission Electron Microscopy

3.2 Scanning Electron Microscopy
and Chemical Etching Results

4. Discussion

5. References

6. Figures

Technical Report No. 2 - Table of Contents

Residual Saw Damage in Silicon Wafers and
Its Influence on MOS Capacitance Relaxation

1. Introduction

2. Experimental

 2.1 Fabrication of MOS Capacitors

 2.2 Electrical Apparatus

 2.3 Data Collection

 2.4 Measurements

 2.4.1 H-Wafers versus V-Wafers

 2.4.2 HF Treatment

 2.4.3 Polishing Parameters

 2.4.4 Wafer Position

2.4.5 Czochralski versus Float
Zone Crystals

3. Discussion

4. List of References

5. Figures

Technical Report No. 3 - Table of Contents

Chapter 1

Damage Profiles in Silicon Wafers
After ID Slicing

1. Introduction

2. Depth of Saw Damage Measurements

2.1 Review of Mechanically Induced
Damage in Silicon After Slicing

2.2 Surface Damage Models

3. Problems of Mechanical Damage Studies

4. Damage Measurements

4.1 Experimental Approach

4.2 Measurements of Damage

4.3 Damage Profiles

5. Application of Saw Damage Measurements
to H- and V-Silicon Wafers

6. Discussion

7. Summary and Conclusions

8. References

Chapter 2

Fracture Strength of Doped Single
Crystal Silicon

1. Introduction

2. Experimental Approach

3. Technique Development

4. Measurements of Fracture Strength on Seed
and Tail Sections of Silicon Crystals

5. Conclusions

6. References

Technical Report No. 4 - Table of Contents

Chapter 1

Bulk and Surface Effects in
Damaged Silicon Surfaces

1. Introduction

2. Experimental

 2.1 Fabrication of MOS Capacitors

 2.2 Procedure for Surface Damage
 Generation

3. Results: Structural Investigations

3.1 ISS Damage in Silicon Surfaces

After Device Processing

3.2 ISS Damage in Silicon Surfaces

After Device Processing

3.3 Surface Topography of Impact

Sound Stressed Silicon Surfaces

After Device Processing

4. Results: Electrical Measurements

5. Summary and Conclusion

6. References

Chapter 2

Generation-Lifetime in Damage-

Free Silicon Surfaces

1. Introduction

2. Ribbon Growth

3. Electrical Measurements

4. Summary

5. References

Technical Report No. 5 - Table of Contents

Chapter 1

The Closed Boat: A New Approach for Semiconductor
Batch Processing

1. Introduction

2. Experimental Procedure

3. Results

3.1 Temperature Gradient Measurements

3.2 Crystals Perfection During Batch Processing

3.3 Wafer Warpage During Batch Processing

4. Batch Processing of Silicon Slabs

5. Discussion

6. Summary

7. References

Chapter 2

**A New Fast Technique for Large-Scale Measurements
of Generation Lifetime in Semiconductors**

Introduction

Theoretical

Experimental and Results

Summary

References

Technical Report No. 6 - Table of Contents

Chapter 1

**Computer Generation of Kikuchi Maps for
Transmission Electron Microscopy (TEM) and
Scanning Electron Microscopy (SEM)**

Investigations

by H. Kappert

Introduction

Geometry

Orientation

The Program

Selection of Diffraction Planes

Transition of Desired Orientation

Rejection of High Index and High Order Planes

Calculation of Coordinates

Determination of Radius and Center of Kikuchi Circle

Provision for au (x,y) Array for the Plot

Plotting Section

Plotting the Pole Map

Results

References

Appendix: Program in Fortran IV for IBM 1800 Computer

Chapter 2

**Electrical Characterization of Quasi MOS
Structures on Silicon**

by W.R. Fahrner, E. F. Gorey, and C. P. Schneider

Introduction

Analysis of Equivalent Network

Spreading Resistance vs. Dot Diameter

Range of Quasi MOS Capacitance Technique

Comparison With Other Techniques

Results and Discussion

Summary and Conclusions

References

Technical Report No. 7, Part I - Table of Contents

Chapter 1

**Growth Kinetics of Stacking Faults
in Oxidized Silicon**

by K. Yang, G. H. Schwuttke, and H. Kappert

1. Introduction

2. Experimental Approach

3. Results: Experimental and Theoretical

3.1 Growth Kinetics of Stacking Faults

3.2 Oxidation of Parameters

3.3 Effects of Oxide Thickness

3.4 Stacking Fault Growth Model

4. Discussion

5. Summary

6. Appendix: Growth Model Theory

References

Chapter 2

Lifetime Control in Silicon

Through Impact Sound Stressing (ISS)

by G. H. Schwuttke and K. Yang

1. Introduction

2. The ISS Technique

3. Procedure for ISS Surface Damage Generation

4. Survey of ISS Damage

5. Lifetime Improvement Through ISS

5.1 Experimental

5.2 Results

5.2.1 Substrates

5.2.2 Expitaxial Films on ISS'ed Substrates

5.2.3 Epitaxial Films on Ion-Implanted Substrates

6. Discussion

7. Summary

References

Appendix

Technical Report No. 7, Part II - Table of Contents

Chapter 1

Damage Removal on Silicon Surfaces:
A Comparison of Polishing Techniques

by G. H. Schwuttke and A. Oster

Introduction

Experimental

Chemical Polishing

Chem-Mech Polishing

Cupric Ion Chem-Mech Polishing of Silicon

Silicon Dioxide for Chem-Mech Polishing of Silicon

Experimental Procedure

Results

Damage Topography and Damage Depth

Chemical Etching

Chem-Mech Polishing

Cupric Ion Polishing

Silicon Dioxide Polishing

Discussion

Summary

Acknowledgment

References

Chapter 2

**Defect Profiles in Silicon After
Impact Sound Stressing**

by H. Kappert, G. H. Schwuttke, and K. Yang

Introduction

Experimental

Results

- 1. Optical Survey of ISS Damage**

- 2. Transmission Electron Microscopy (TEM) of
ISS Damage**
 - 2.1 Fracture Cones - General Observations**

 - 2.2 TEM of Fracture Cones - Dislocation Analysis**

3. TEM Analysis of Abrasion Damage

3.1 Post ISS Properties of Grooves

3.2 Post Annealing Properties of Grooves

3.2.1 Stacking Fault Nucleation Through
Prismatic Loops

3.2.2 Stacking Fault Nucleation Through
Microsplits

3.2.3 TEM Analysis of Oxidation Induced
Stacking Faults

4. TEM Analysis of Oxidation Induced Stacking
Faults

4.1 Analysis of Partial Dislocation

4.2 Analysis of Stacking Fault Nature

Discussion

Summary

Acknowledgment

II. Contract No. N00173-76-C-0303

Technical Report No. 1 - Table of Contents

**Minority Carrier Lifetime and Defect Structure
in Silicon After Cesium Implantation**

by G. Sixt, H. F. Kappert and G. H. Schwuttke

Introduction

Experimental

Sample Preparation

Electrical Measurements

SIMS and TEM Measurements

Results

Discussion

Nucleation and Annealing of Defects

Defects and Minority Carrier Lifetime

Summary

Acknowledgments

References

Appendix

Technical Report No. 2 - Table of Contents

Minority Carrier Lifetime in Annealed
Silicon Crystals Containing Oxygen

by K. H. Yang, H. F. Kappert and G. H. Schwuttke

1.0 Introduction

2.0 Experimental

3.0 Swirl Defects and Minority Carrier Lifetime

3.1 Electrical Measurements in Substrates

3.2 Formation of Swirl Defects in Substrates

3.2.1 Oxygen Concentration and Swirls

3.2.2 Analysis of Swirl Defects in Dislocation-Free Crystals

Chemical Etching and X-ray Topography

Transmission Electron Microscopy of Precipitates

Transmission Electron Microscopy of Dislocation Loops

Transmission Electron Microscopy of Stacking Faults

3.2.3 Analysis of Swirl Defects in Dislocated Crystals

Chemical Etching

Transmission Electron Microscopy of Precipitates

Transmission Electron Microscopy of Stacking Faults and Dislocation Loops

3.3 Electrical Measurements in Epitaxial Layers

3.4 Defect Studies in Epitaxial Layers

3.5 Oxygen Influence on Diode Performance

4.0 Discussion

5.0 Summary

6.0 Acknowledgments

7.0 References

Appendix

APPENDIX II(a)

IMPACT SOUND STRESSING (ISS) OF GaAs WAFERS*

by R. G. Dessauer and E. Hearn

This report describes the application of ISS for GaAs wafers. The intent of this investigation is to develop a technique for III - V compounds capable of introducing, in a controlled manner, damage into crystal surfaces. This will provide a means not only for the study of damage propagation in such crystals, but also for investigation of possibilities of damage gettering in III - V compounds.

1. ISS EQUIPMENT

The Impact Sound Stressing (ISS) technique used for silicon (1) has been adapted for the introduction of microdamage into GaAs surfaces. The brittle nature of the material and the irregular sizes and shapes of wafers mandate certain pertinent process and equipment changes.

The non-circular, non-uniform shape of GaAs single crystal wafers is due to the horizontal zoning growth process. This process is generally used for the production of standard

*Developed under Air Force Contract No. F19628-75-C-0174

quality material. It results in a single crystal ingot having the shape of the containing boat. The size and shape of wafers cut economically from such an ingot are thus determined by the quantity of material placed in the boat, its shape, and the slicing direction. Non-uniform wafers are accommodated in the ISS apparatus by mounting them on circular membranes which are then placed into the apparatus.

The flexural stresses induced in the brittle wafers and the mounting material, during ISS, are reduced by placing the sample carrier membrane away from the source of sound. This arrangement protects against wafer breakage and avoids detachment of the samples from the membrane. It permits the convenient use of wax for sample mounting.*

A similar membrane, but without a sample attached, is used as the driver. The driver membrane impels the tungsten balls against the sample mounted on the carrier membrane above, thus producing the microdamage.

1.1 Equipment Description

A schematic representation of the apparatus is given in Fig.

1. A photograph of the actual equipment as in operation is

*Recently, a vacuum system has been successfully used to hold samples on the sample carrier membrane during ISS.

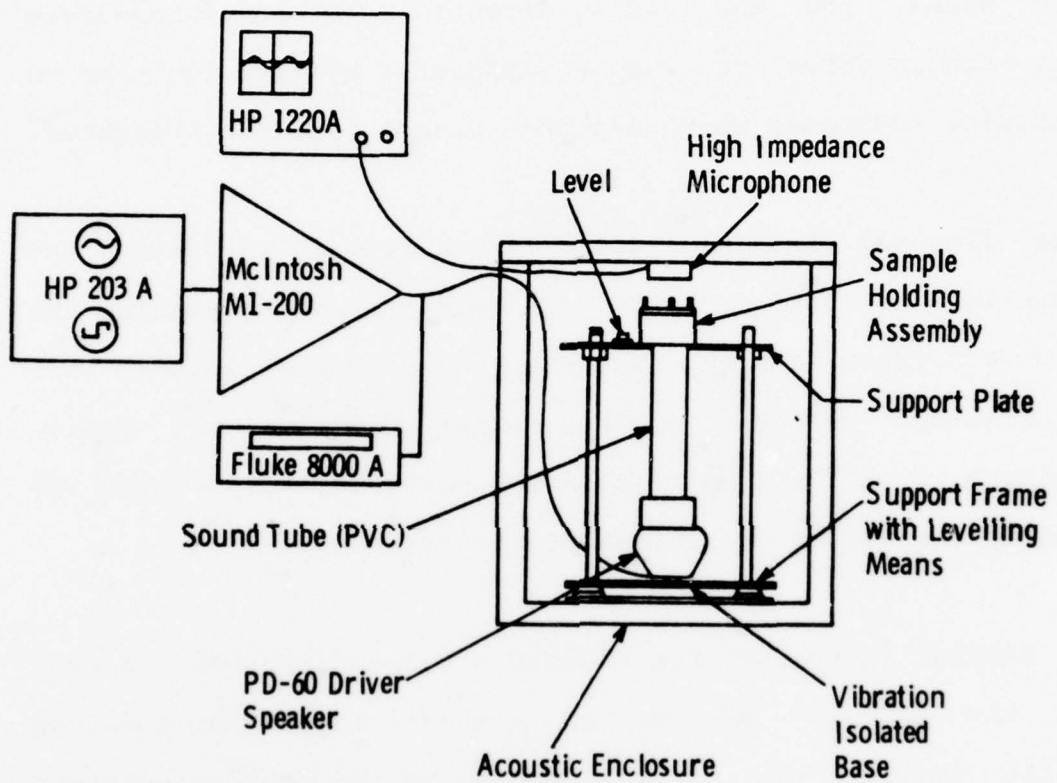


Fig. 1. Schematic of Impact Sound Stressing (ISS) apparatus for GaAs.

shown in Fig. 2a, with the acoustic enclosure containing the ISS unit to the right of the controls console containing the electronic equipment. An additional view showing the apparatus within the acoustic enclosure is given in Fig. 2b. The source of sound is the driver portion of a loud-speaker (Atlas Model PD-60T/60 watt), operated by a MacIntosh M1-200 power amplifier. Input power to the acoustic driver is monitored by a Fluke 8000A digital multimeter for coarse setting to avoid overdriving. A Hewlett-Packard HP 203A function generator provides the sinusoidal oscillation. This equipment is also capable of producing square wave pulses.

The sound tube is a polyvinyl chloride (PVC) pipe attached to the driver by a threaded PVC coupling. The sample holder assembly is threaded to the top end of the sound tube. The effective length of tube, coupling the driver membrane in the sample holder assembly to the driver, is approximately 35 cm. The assembled unit is suspended in the support frame. The support plate rests on adjustment nuts threaded on the three symmetrically placed support rods. This three-point suspension is used to level the apparatus. A button type bubble level placed on the support plate serves as level indicator. The support frame rests on a base equipped with four vibration isolators. It is located in

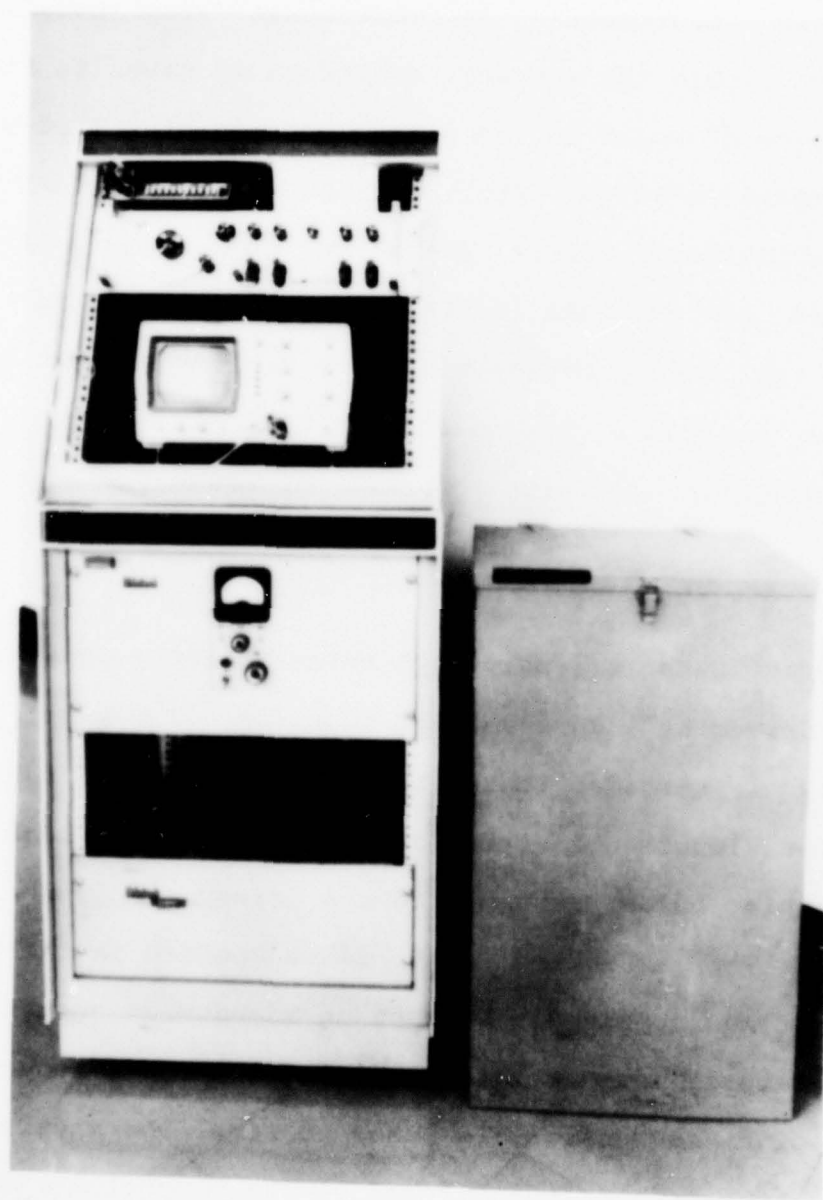


Fig. 2a. Photograph of instrumentation corresponding to Fig. 1 (acoustic enclosure at right).

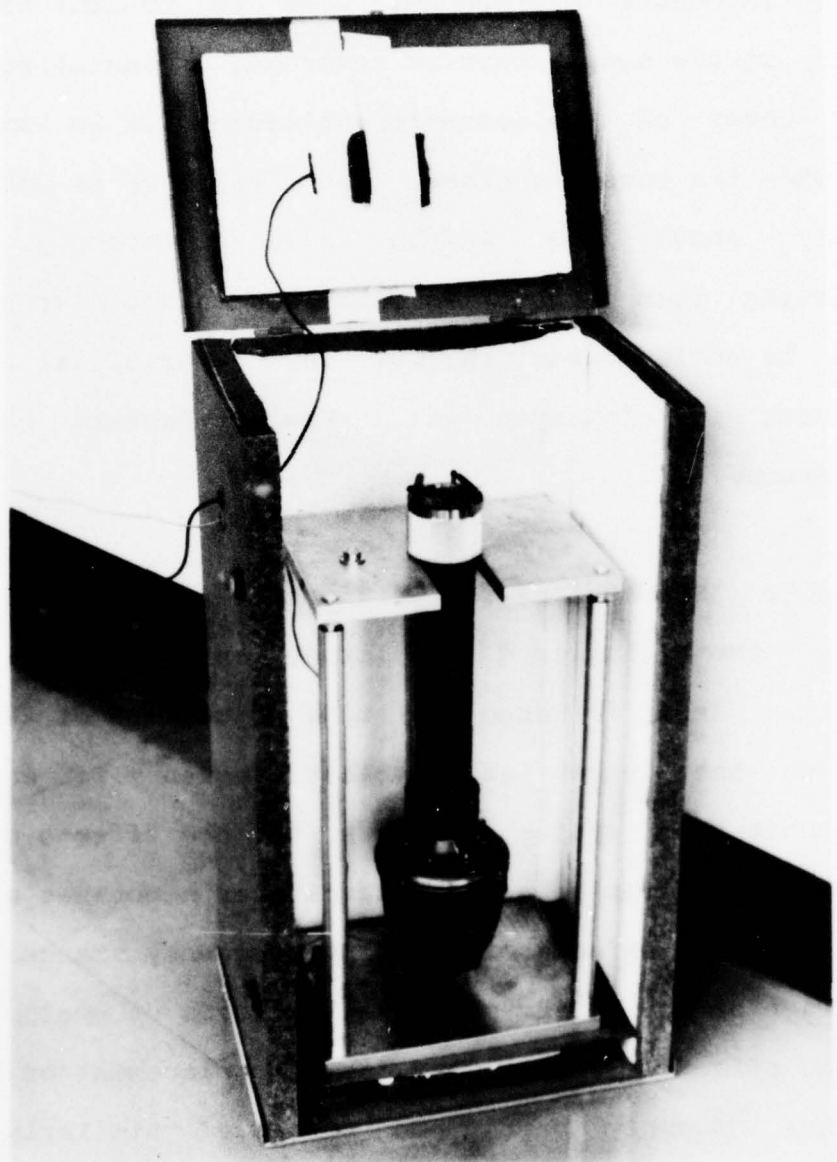


Fig. 2b. Equipment within acoustic enclosure.

the acoustic enclosure which reduces environmental sound to levels acceptable in open laboratory or manufacturing areas. A high impedance microphone, used to monitor the sound emitted at the sample carrier membrane, is installed in the hinged cover of the acoustic enclosure. It is located so that when the cover is closed the microphone is positioned directly above the sample holding assembly. Sound attenuating foam rubber is installed on the microphone as needed to avoid overdriving it. The output signal from the microphone is displayed on a Hewlett-Packard HP 1220A oscilloscope.

Repeatable ISS action for different runs is achieved by keeping the displayed amplitude on the oscilloscope constant. This is done by fine adjustment of the input power to the driver at resonant frequency for each run. This monitoring system corrects for the effects of small differences in samples and sample carrier membranes and also neutralizes the effects of resonant frequency changes caused by aging of the driver membrane. Effects of small changes in the effective tube length due to replacement of drivers or other assembly parts are corrected similarly. The oscilloscope also aids in accurately finding the resonant frequency.

A detailed sketch of the sample holding assembly is given in Fig. 3, and a photograph of the actual unit, as in operation, is shown in Fig. 4a. In Fig. 4b the sample carrier clamping ring and membrane have been removed, and the membrane with a sample mounted is displayed above the unit. The tungsten balls are seen resting on the driver membrane.*

The impact chamber containing the tungsten balls is formed by the two membranes and the membrane clamping ring. The driver membrane is clamped into the coupling by the membrane clamping ring, which is fastened to the coupling by three screws. In Fig. 3, the sample is shown mounted on the sample carrier membrane, which rests in the top of the membrane clamping ring. The membrane is held securely in place by the sample carrier clamping ring. This ring distributes the holding force exerted by three spring clips located 120° apart around the membrane clamping ring. The spring clips may be swivelled away to facilitate removal of the sample carrier clamping ring and membrane for sample

*The balls are approximately 0.3 mm in diameter and, in order to avoid repeated counting, several quantities were weighted. Figure 5 shows the correlation of weight to the number of balls. The slope of the line gives the weight of one ball. This graph may be used to weight out the correct number of balls to within $\pm 0.05\%$.

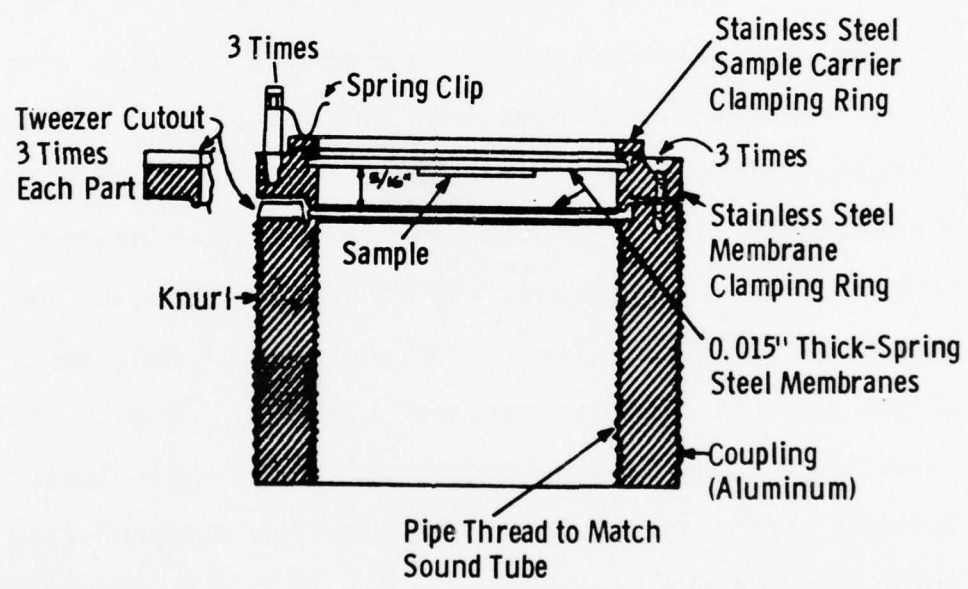


Fig. 3. GaAs sample holding assembly for ISS.

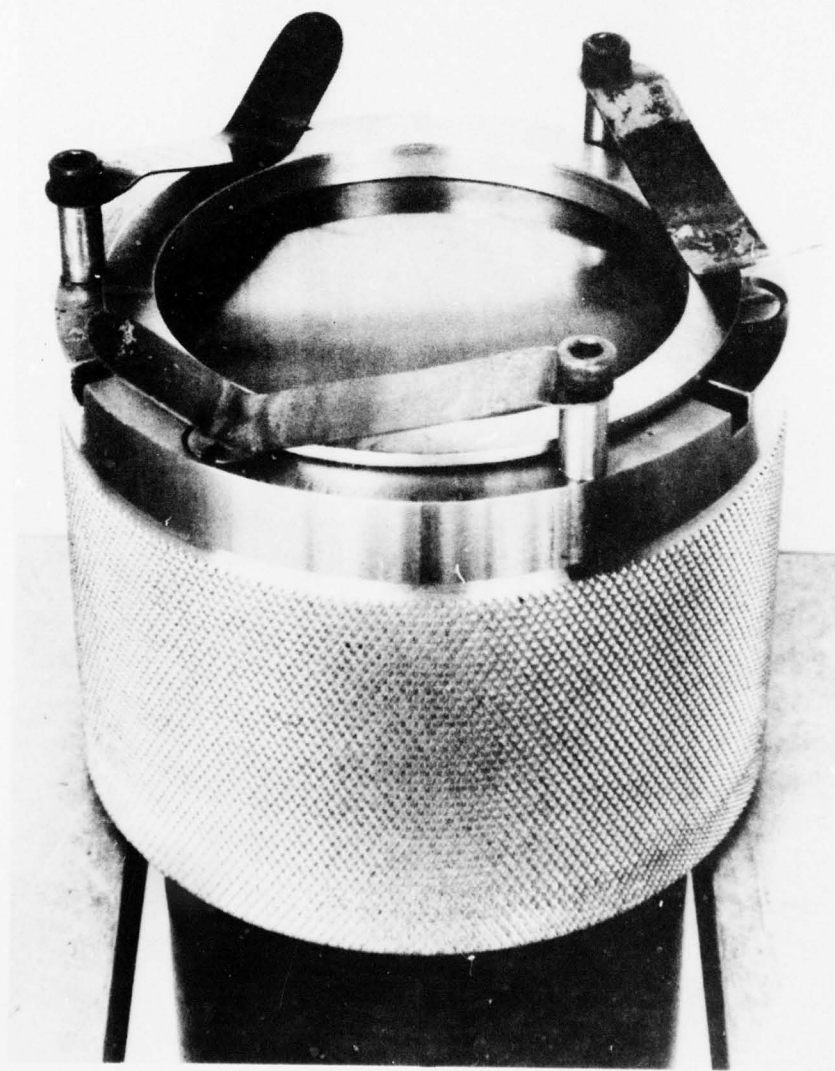


Fig. 4a. Photograph of assembly corresponding to Fig. 3.

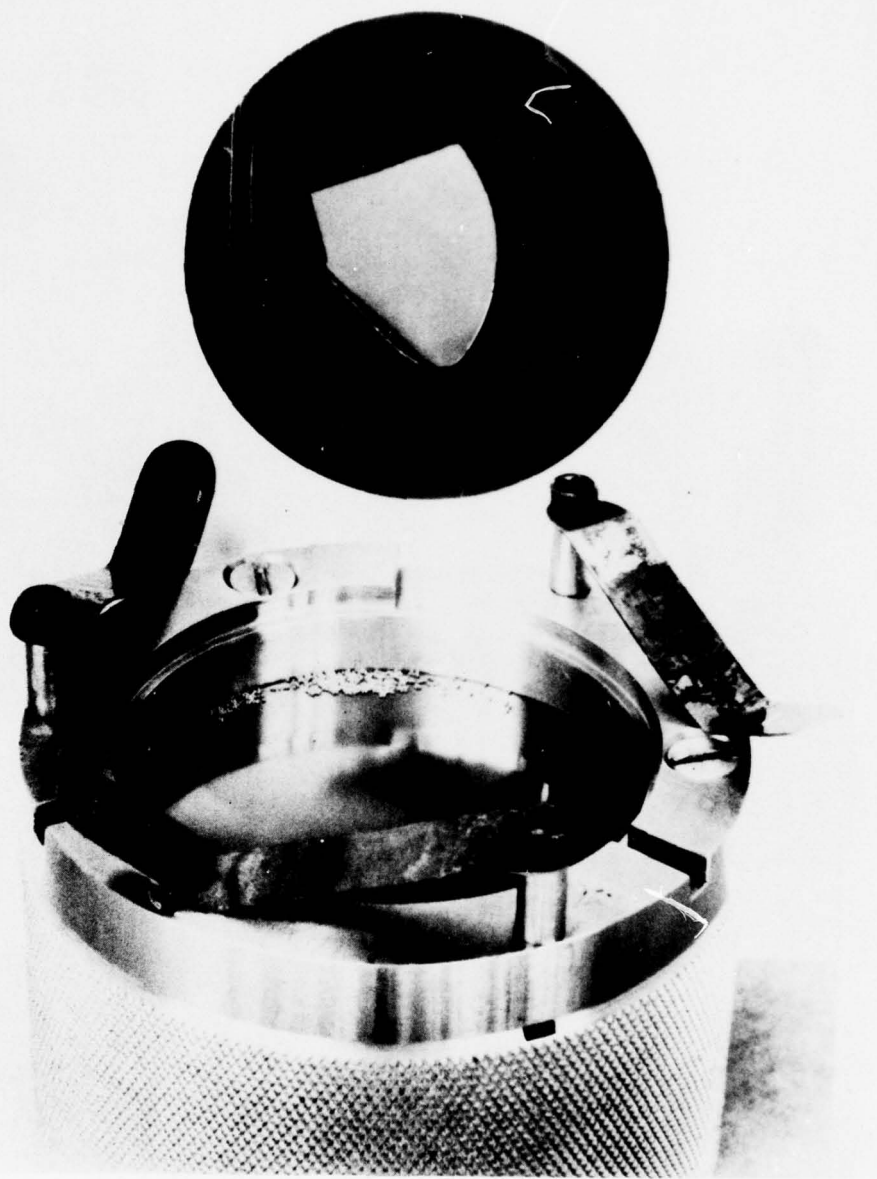


Fig. 4b. Assembly open, loaded with tungsten
balls. Sample carrier membrane with
sample above.

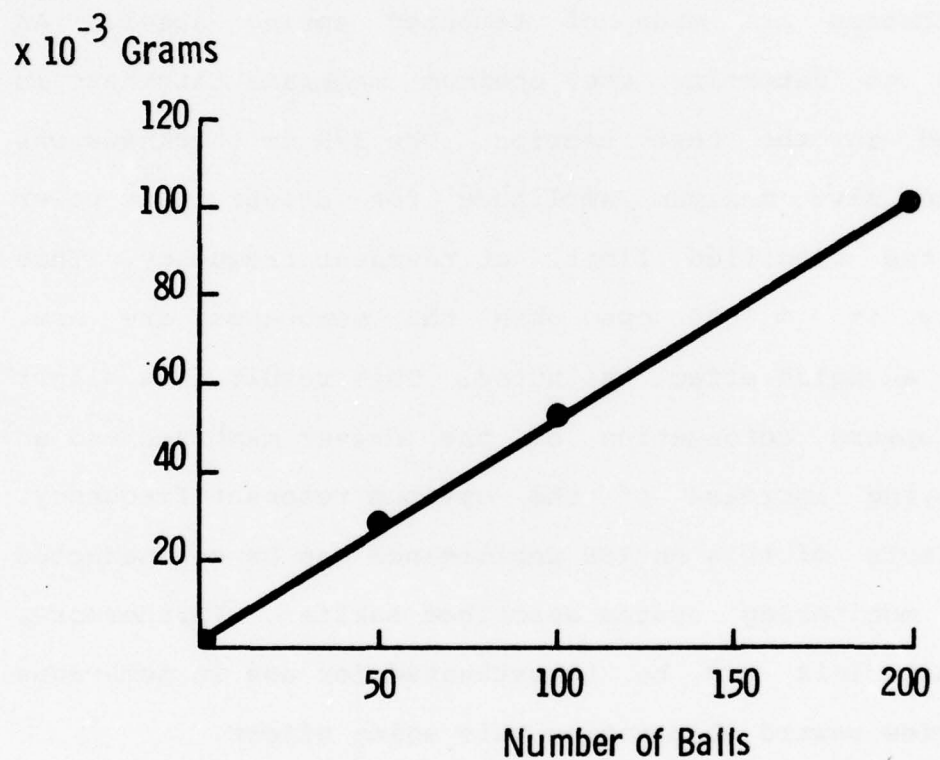


Fig. 5. Plot of weight vs. number of balls. Slope gives a value of 0.0005 g for a single ball.

changes. Cutouts are provided in the membrane clamping ring and coupling to facilitate removal of the membranes. A knurl is provided on the outside of the coupling to facilitate installation on the sound tube, which threads into it.

The membranes are made of tempered spring steel. An analysis to determine the optimum membrane thickness is presented in the next section. The 3/8 mm thickness was found to give maximum amplitude for driver input power within the specified limit, at resonant frequency. This frequency is \sim 1000 cps when the membranes are new. However, an aging effect was noted. This result in a slight convex upward deformation of the driver membrane and an accompanying increase of the optimum resonant frequency. Any effects of this on ISS performance can be counteracted by the monitoring system described earlier. Furthermore, other materials may be investigated for use in membranes with a view toward eliminating this aging effect.

1.2 Determination of Membrane Dimensions

A convenient membrane diameter of 5.5 cm free (unclamped) was chosen. The optimum membrane thickness was then determined by analysis.

Membrane oscillations and the occurrence of resonant modes of the driver membrane were measured using a transducer. The transducer, whose output was fed to an oscilloscope, was first placed over the impact chamber without the sample carrier membrane in place. The frequency was scanned at a driver input power (10 watts) compatible with the sensitivity of the transducer. The position and amplitude of the fundamental and harmonic modes were plotted. Results for various membrane thicknesses are given in Figs. 6-9. These results are helpful in the choice of membrane thickness.

The measurement was repeated with the sample carrier membrane, the tungsten balls, and the sample to be stressed in place. The results showed a negligible change in frequency but a large change in amplitude. This indicates that, in the fully assembled configuration, the oscillations are damped but the resonance of the system is maintained.

The criterion of maximum coupling led to the selection of the 3/8 mm thick membrane at a frequency of \sim 1000 Hz.

One long term change observed was the membrane aging effect mentioned earlier. Increasing resonant frequency was coincident with a gradually increasing, permanent bowing

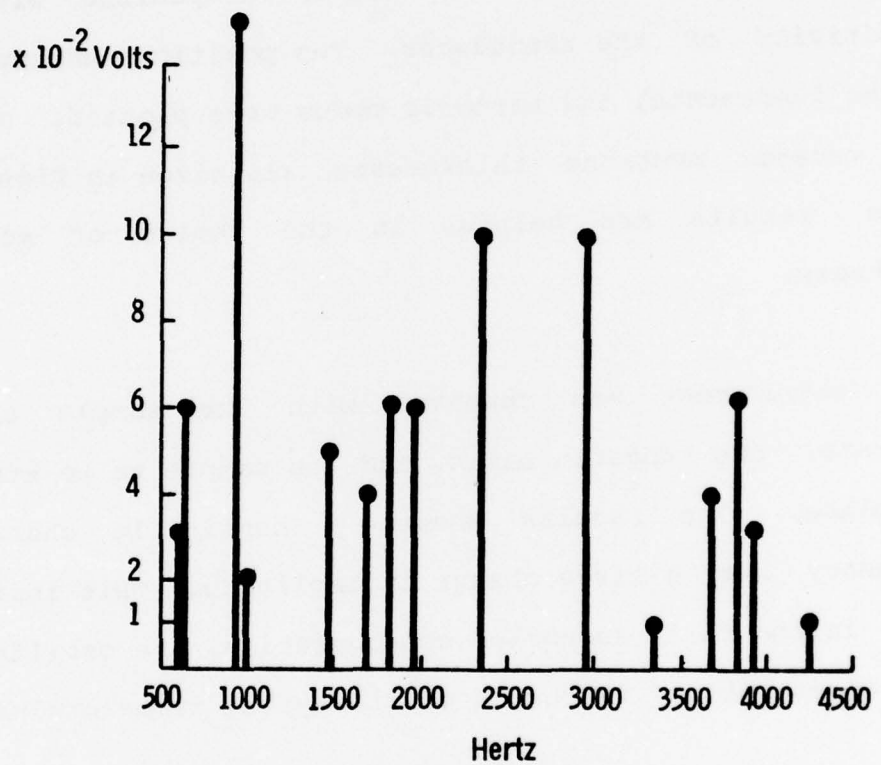


Fig. 6. Output vs. frequency of a 1/8 mm steel diaphragm.

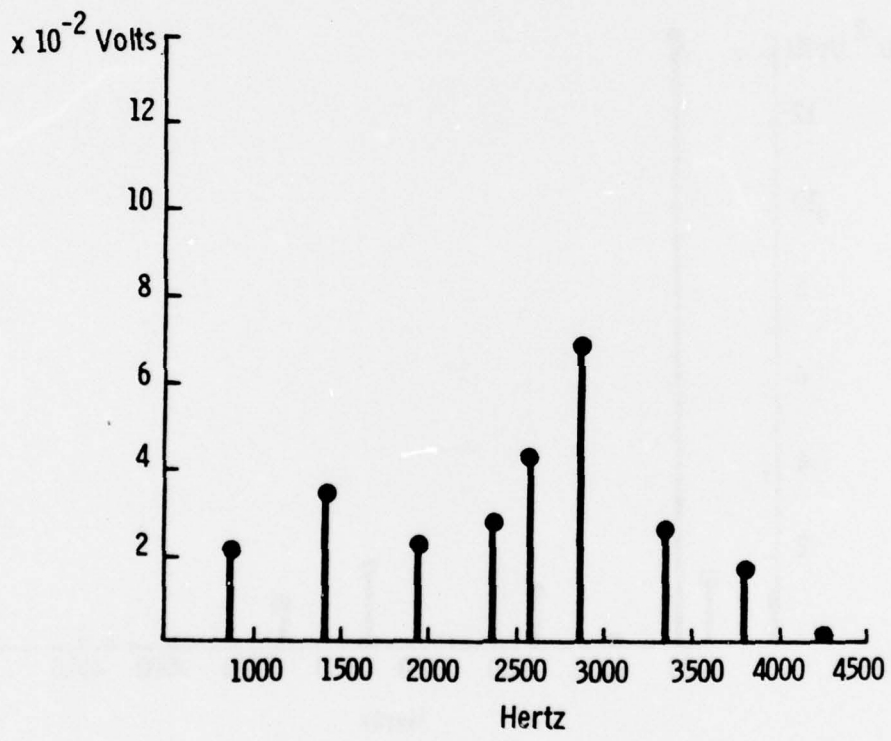


Fig. 7. Output vs. frequency of a 1/4 mm steel diaphragm.

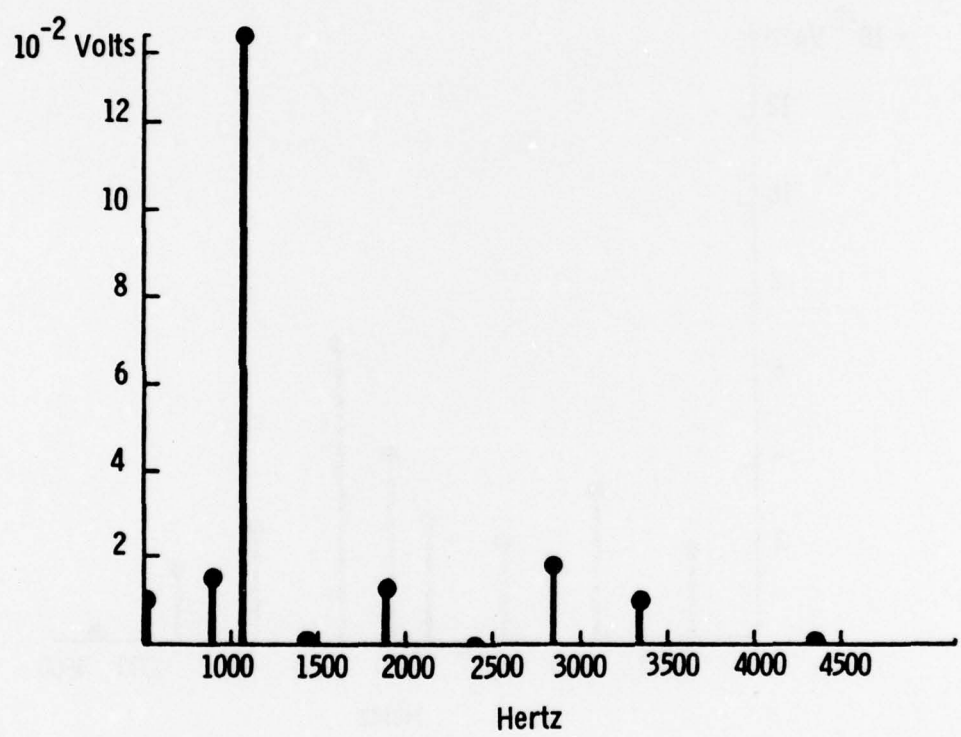


Fig. 8. Output vs. frequency of a 3/8 mm steel diaphragm.

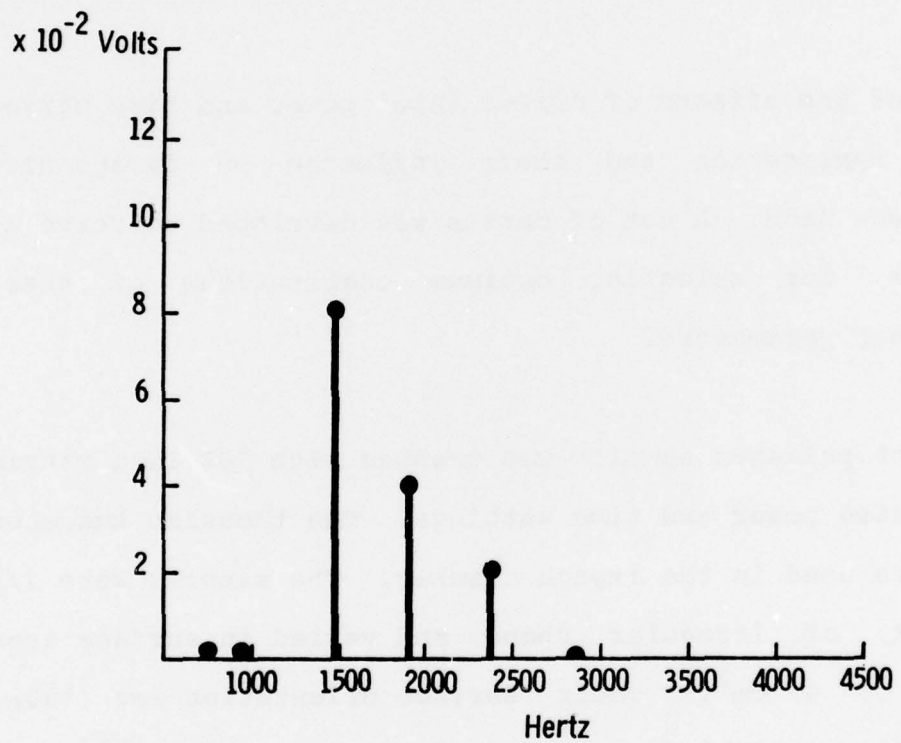


Fig. 9. Output vs. frequency of a 1/2 mm steel diaphragm.

away of the membrane from the driving force. A change of +400 Hz had occurred after about ten hours of operation. The frequency appeared to stabilize at about 1530 Hz, after continued use.

1.3 Evaluation of ISS Operational Parameters and Damage Site Density in GaAs Slices

A study of the effects of driver input power and time period of ISS application and their influence on damage site density was made. A set of curves was developed to serve as a guide for selecting optimum combinations of these operational parameters.

A group of polished samples was treated with ISS in a matrix of selected power and time settings. One thousand tungsten balls were used in the impact chamber. The samples were 1/2 mm thick, of irregular shape, and varied in surface area from 1 to 4 cm². Their surface orientation was (100), resistivity: 0.00349 Ω-cm, and doping: Sn - 6.5 x 10¹⁷.

1.3.1 Matrix Determination

Initial experiments provided guidelines for the selection of practical values in the matrix. The experiments showed that

excessive driver input power causes a catastrophic pulverization of the GaAs surface by the tungsten balls. At the lower power limit the balls fail to fracture the surface due to insufficient energy imparted to them by the driver membrane. An excessively long time period results in overlapping of damage site boundaries preventing density determination. It may also have a minor effect on surface pulverization due to increased probability of repeated impacts at the same site. Time conservation is also considered in the setting of the time period upper limit. The lower limit of time was selected to provide sufficient damage site density for microscopic studies. Sample thickness was considered to avoid breakage at higher power levels.

The experimental matrix selected is given in Table I:

TABLE I. Experimental Matrix - Driver Input Power versus Time Period of ISS Application

Time (sec.)	Power (watts)			
	10	15	20	25
30	Run 1	Run 2	Run 3	Run 4
45	Run 5	Run 6	Run 7	Run 8
60	Run 9	Run 10	Run 11	Run 12
75	Run 13	Run 14	Run 15	Run 16

1.3.2 Damage Site Density Determination

A photomicrograph (magnification: 46X) was recorded of the ISS treated surface of each sample processed in the matrix. The number of damage sites visible within a sixteen square centimeter area on each micrograph were counted. The count was performed independently by three individuals and the three sets of statistics were averaged. The results were used to calculate the density, using the simple equation: $d = N (m)^2 / 16$; where d = density (sites/cm^2), N = number of sites per 16 cm^2 area on micrograph, and m = magnification of micrograph.

1.3.3 Matrix Data Analysis

Damage site density obtained from fourteen of the sixteen runs is plotted vs. time period of Fig. 10. Data from runs 15 and 16 was omitted since it appeared to be spurious.

Constant power curves are fitted to the data points. The curves are shown terminated at the matrix time limit of 75 seconds. These curves could be extended, however, since greater densities are possible with longer time periods. Several subsequent runs made at 12.5 watts for 200 seconds yielded a density of $492 \times 10^2 \text{ sites/cm}^2$. The non-linear

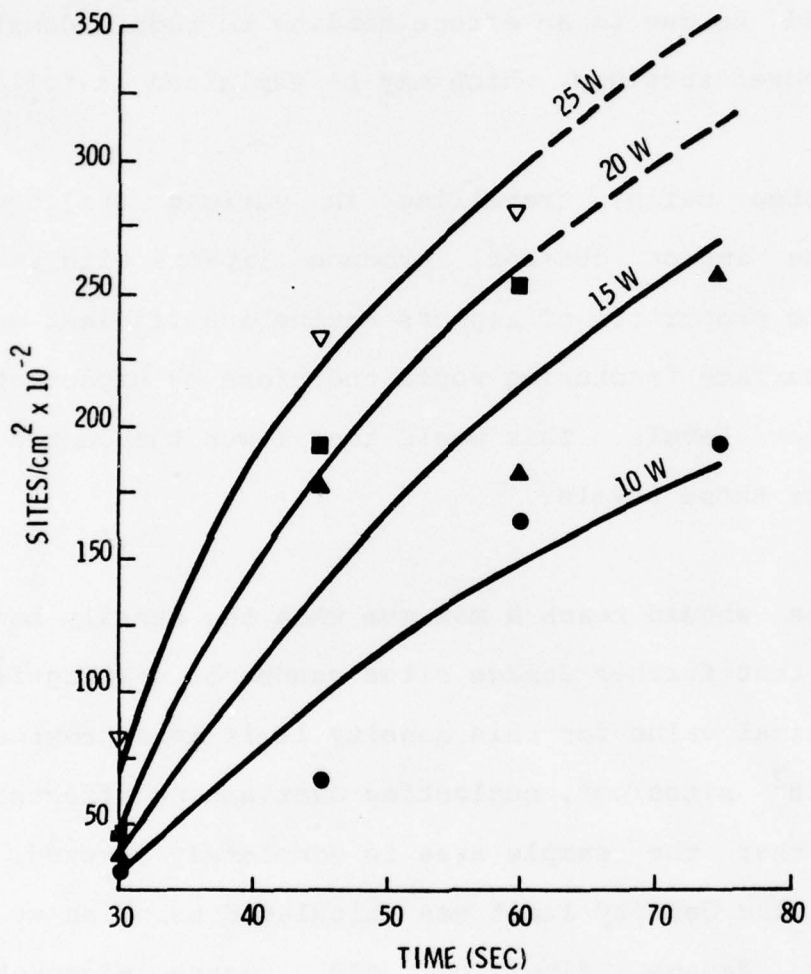


Fig. 10. ISS application time period vs. damage site density at various driver input power levels.

shape of the curves may be due to increased overlapping of damage sites, at higher values of time and power. This would reduce the density count at those values to less than the actual impact density. The lower power curves appear to be flatter, with 10 watt curve approaching a straight line. This could be due to an effect tending to reduce densities at lower power settings, which may be explained as follows.

The tungsten balls, travelling in various trajectories within the impact chamber, produce impacts with unequal force. The proportion of impacts having insufficient energy to cause surface fracturing would therefore be higher at the lower power levels. This would then lower the damage site density for those levels.

The curves should reach a maximum when the density becomes so high that further damage sites cannot be distinguished. A theoretical value for this density limit is approximately 1670×10^2 sites/cm², neglecting overlapping effects, but assuming that the sample area is completely covered. The value for the density limit was calculated using an average area per damage site of 600 square micrometers. Distinguishable overlapping of damage sites could raise this value by a factor of three. It appears possible, however, that the balls impact the surface in certain patterns

depending on the oscillating frequency. This could cause certain sample areas to remain low in damage for all practical time periods. Such an effect would set a lower countable density limit. In either case, densities approaching the limiting values may be expected to have considerable effect on the severity and variation of damage. This would be due to the high probability of repeated coincidence of ball impact sites.

In this section it is shown that while application time is the major factor influencing damage site density, driver input power also affects it. This may be due to changes in ball velocities resulting in variation of the number of impacts per unit time.

The curves in Fig. 10 indicate that both time period and input power influence the damage site density. An additional analysis of the experimental data was made to determine the relative effect of these two operating parameters.

Pairs of matrix runs made at equal power levels for different time periods were selected. The percent increase in time and the resulting increase in damage site density from the shorter to the longer run were determined. The

average density increase for all pairs with the same time increase percentage, but at different power levels per pair, was calculated. This provides a measure of the influence of time alone, which is shown as curve I in Fig. 11.

Conversely, pairs of runs made for equal time periods, at different power levels, were selected. The percent increase in power and the increase in damage site density were

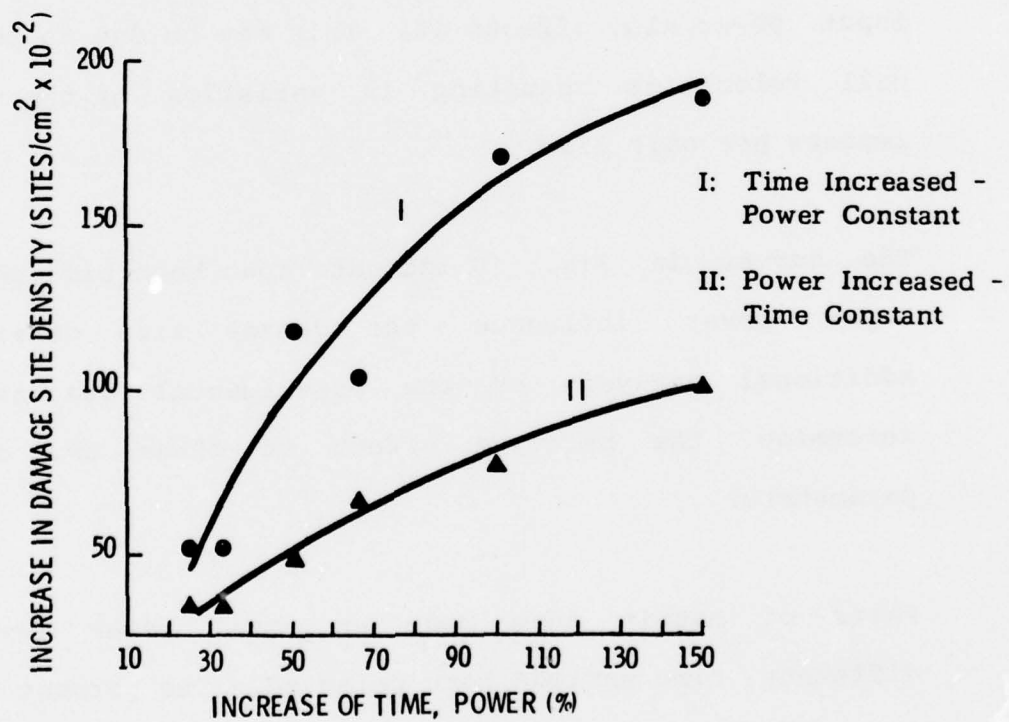


Fig. 11. Damage density vs. time dependency.

determined similarly. The average density increase for all pairs with the same power increase percentage, but run for different time periods per pair, gives a measure of the influence of driver input power alone. This is given with curve II in Fig. 11.

It can be seen from the plots that the length of time period has a greater influence on damage site density than has driver input power. This is shown by the location of curve I above curve II. Their positions on the graph indicate that the relative importance of time to power is about 2:1. The non-linear shape of these curves may be due to the increased probability of overlapping of impact sites when the time or power difference between the runs considered is increased. This would result in a decreased difference in density count. This effect is greater for time, as evidenced by the greater instantaneous slope of curve I, and should be in proportion to the greater influence of time on damage site density.

1.3.4 Summary for Selection of ISS Operational Parameters

The curves in Fig. 10 may be used as a guide in the selection of driver input power and time period of ISS

application for given damage site densities. It must be kept in mind, however, that they may be considered valid only for the equipment and frequencies described in Sections 1.1 and 1.2, and the material described in Section 1.3. The pertinent numerical values are summarized in Table II.

TABLE II. Sample, Equipment and Operational Parameters Used for ISS Treatment of Gallium Arsenide

Parameter	Value
<u>Sample</u>	
Surface orientation	(100)
Thickness	1/2 mm*
Surface area	1-4 cm ²
Resistivity	0.00349 Ω-cm
Doping	Sn-6.5x10 ¹⁷
<u>Equipment</u>	
Sound tube effective length	~ 35 cm
Sound tube inside diameter	4.7 cm
Impact chamber height	8 mm
Impact chamber diameter	5.5 cm
Membrane free diameter	5.5 cm
Membrane thickness	3/8 mm
Ball diameter	~ 0.3 mm
<u>Operational</u>	
Number of balls	1000
Frequency (with new membranes)	~ 100 c/s
*Sample (1 cm x 1 cm squares) as thin as 1/4 mm been run at 12.5 watts without breakage	

Damage site density requirements depend upon the purposes for which the ISS treated material is to be used. Most requirements probably fall within the range of 15K to 30K sites/cm². However, as mentioned earlier, densities approaching 50K sites/cm² have been obtained.

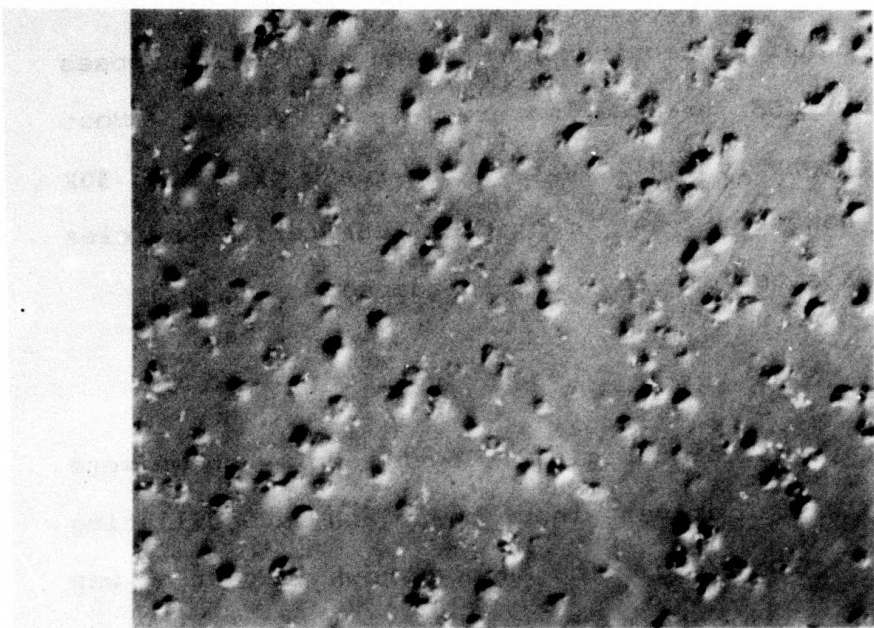
Two examples are given in Fig. 12. Both samples shown were run at 12.5 watts driver input power and an oscillating frequency of 1.53 kc/sec. The sample shown in part a. was run for 50 seconds; the other one for 200 seconds. The density difference is quite apparent in these micrographs.

2. DAMAGE CHARACTERIZATION

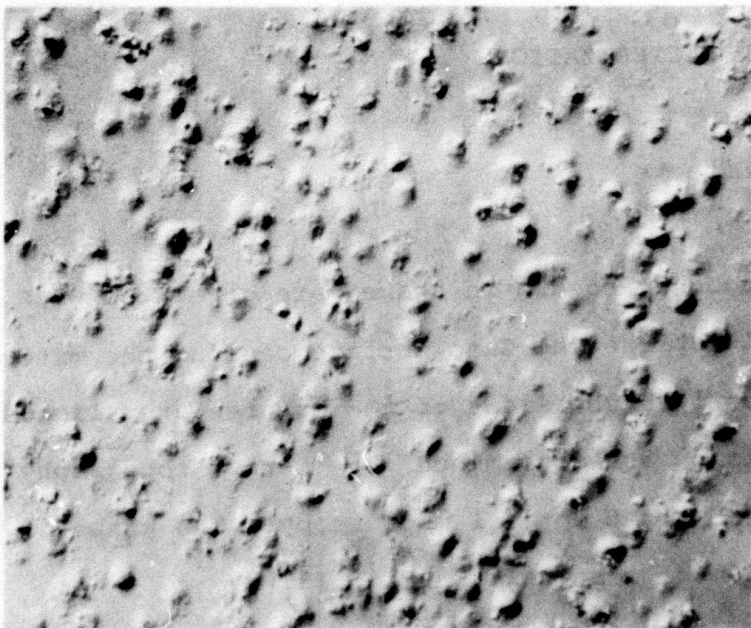
2.1 Surface Effects

Depressions, roughly square in shape, are generated when the tungsten balls strike the GaAs surface causing the material to yield locally. The sides of the squares are aligned in [110] directions as determined by x-ray topography in conjunction with light optical microscopy. The shape of the damage sites can be seen well in Fig. 13.

The damage sites seen in the relatively low magnification micrographs of Fig. 12 have a pitted appearance. Figure 13,



a. 50 sec; 131X magnification.



b. 200 sec; 131X magnification.

Fig. 12. ISS damage on GaAs, 12.5 watts, 1.53 kc/sec at two application time periods.

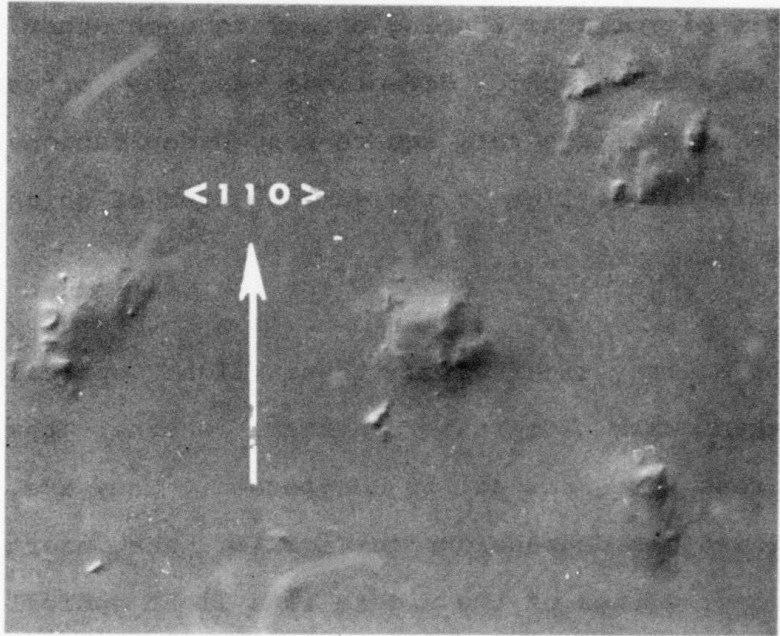
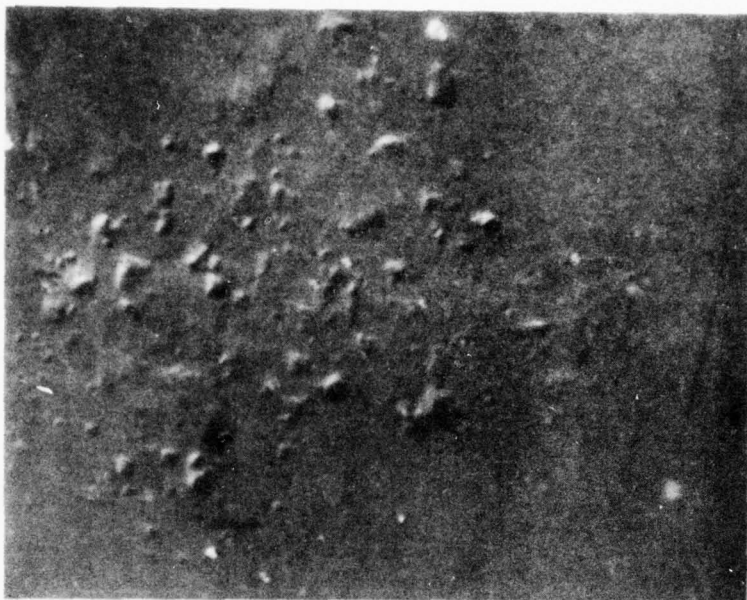


Fig. 13. Crystallographic alignment of ISS damage sites in GaAs; 855X magnification.

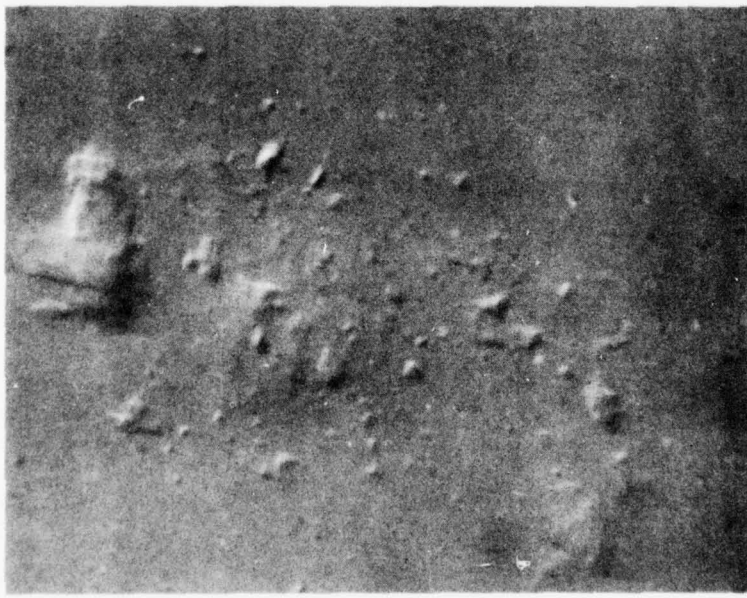
however, indicates a network of fine linear fractures rather than pits. In the highly magnified views of Fig. 14 it becomes apparent that the damage sites consist of numerous clusters of short microcracks running normal to each other, in the same crystallographic directions as the sites themselves. The microcracks form square-shaped depressions on a smaller scale but similar to the damage sites of which they are a part.

It may not be quite clear from these light optical micrographs, taken with Nomarski contrast, whether the square-shaped areas are raised or depressed. They are, however, identified as depressions in Fig. 15. The insert in the lower left corner of the figure is a light optical micrograph (320X magnification) of a square array of ISS induced fractures in GaAs. The main portion of Fig. 15 is a scanning electron micrograph (4300X magnification) of the same array. This shows that the area between the long fractures is a depression rather than a mound as might be concluded from the insert. The SEM illustration also affords a good view of the fine linear fractures running normal to each other, especially near the lower right corner.

A long fracture with curved end can be seen at the right



a. Note: Large fracture with curved
end at right.



b. Note: Two clusters of fractures of varying sizes are visible on edge of damage zone.

Fig. 14. Clusters of micro-fractures forming crystalllographically oriented [110] square arrays at 15% damage zones on GaAs, 1000 \times magnification.

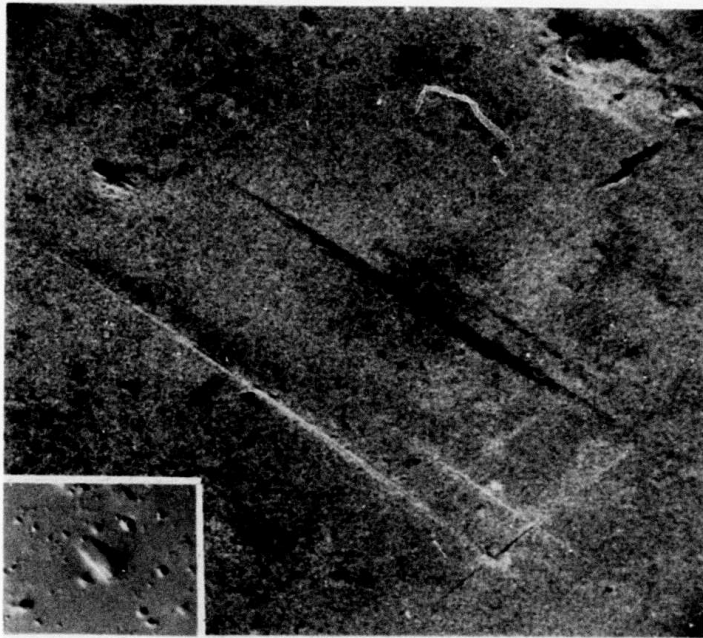


Fig. 15. Scanning electron micrograph of ISS induced square array of microcracks in GaAs; 4300X magnification. Insert shows light optical micrograph of same array; 320X magnification.

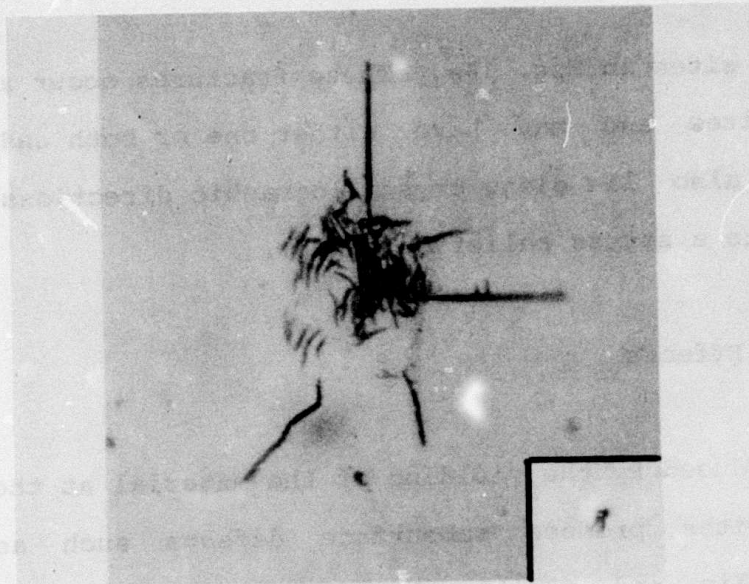
of the damage sites in Fig. 14a. These fractures occur at some damage sites and may have either one or both ends curved. They also lie along crystallographic directions, and may be due to a stress relief mechanism.

2.2 Subsurface Effects

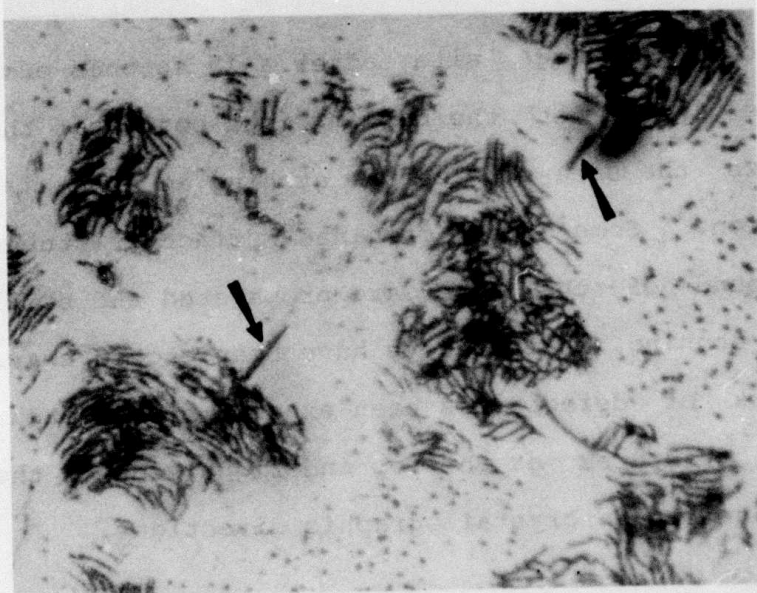
The stresses induced by the yielding of the material at the ball impact sites produce subsurface defects such as dislocations, slip and additional micro-fractures. These defects can be displayed by etching. The etching solution and technique is described in Appendix II(b).

Figure 16a shows a damage site after a 15 seconds etch treatment. The insert at the bottom right corner of the micrograph shows the same site before etching at about 1/5 the magnification. Some of the original surface fractures in the foreground of the site are propagated and still visible after etching, while others have been etched away. A dense network of defects has been exposed by the etch. The two large fractures at the top and right side of the etched damage site run in crystallographic directions.

Another sample, etched for 60 seconds, is shown in Fig. 16b. This displays well the typical intricacy and profusion of the defects below the damage sites. The two fractures,



a. 15 sec. etch; 855X magnification.
Insert: Before etching 167X
magnification.



b. 60 sec. etch; 855X magnification.
Arrows point to fractures aligned
in $\langle 110 \rangle$ direction.

Fig. 16. Etch figures of ISS damage sites
on GaAs.

indicated by arrows, lie in a crystallographic direction.

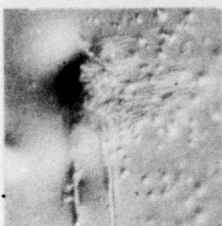
It was noted during repetitive etching that the etch figures of a given damage site first increased in size and then decreased. An example is given in Figs. 17, where the etch figure appears to reach maximum size near steps 4 or 5 and then decreases. (This is also confirmed when the average size of etch figures at the different steps is compared.) The phenomenon indicates that the volume of defect networks generated beneath ISS damage sites is not constant for different levels into the material. Apparently it first expands to a maximum cross-sectional area and then contracts until the deepest extent of the damage is reached. The schematic sketch at the bottom of Fig. 17 illustrates this. The depth of ISS damage varies approximately from 10 to 30 mm for the parameter values investigated, and is discussed in Appendix II(b).

The appearance of the micrographs in Figs. 17 suggests that the etch figures are of uneven height above the general surface. This was investigated by SEM and found to be true. Apparently the damage sites etch at a slower rate than the surrounding undamaged area. This results in the etched defect grooves developing raised rims. It may be noted that etch figures shown in Figs. 16 do not appear to be raised. This is an optical effect obtained by a difference in

**Best
Available
Copy**



a. Before etching.



b. Step 1, 4 sec.



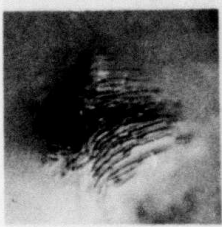
c. Step 2, 8 sec.



d. Step 3, 12 sec.



e. Step 4, 16 sec.



f. Step 5, 20 sec.



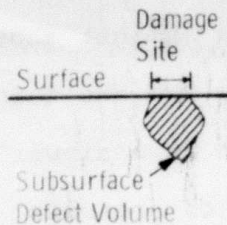
g. Step 6, 24 sec.



h. Step 7, 28 sec.



i. Step 8, 40 sec.



j. Schematic representation
of shape of defect volume
under damage site.

Fig. 17: ISS damage site... Etched repetitively
from 4 to 40 sec.; 1130X magnification

Nomarski contrast setting to accentuate the defect networks.

Detailed electron microscopy studies of ISS damage sites on GaAs surfaces are reported in Chapter 1 of this Final report.

3. REFERENCES

1. ARPA Report No. 4, Contract No. DAHC-72-C-0274.
2. ARPA Report No. 6, Contract No. DAHC-72-C-0274.

APPENDIX II(b)

DEPTH OF DAMAGE INDUCED IN GaAs BY IMPACT SOUND STRESSING
(ISS)

by R. G. Dessauer

1. INTRODUCTION

The controlled introduction of microdamage into polished GaAs surfaces by ISS as described in Appendix II(a) is useful in the study of polishing effects and fracture properties of the material (1). It may also be employed to study effects of microdamage on device properties (2). A knowledge of depth of ISS microdamage is necessary for these applications.

Determination of the depth of damage is made by two separate methods, bevelling and cleaving. In the first method, samples are bevelled and subsequently etched to reveal the extent of damage down the bevel. In the latter method samples are cleaved through damaged sites and the cleavage planes are examined by scanning electron microscope.

*Developed under Air Force Contract No. F19628-75-C-0174

Presently only (100) oriented GaAs samples have been examined for depth of damage.

2. EXPERIMENTAL PROCEDURES

2.1 Bevelling

2.1.1 Bevelling Procedure

The samples to be bevelled are cleaved to a convenient size along crystallographic directions as indicated by the ISS damage. They are between 400 to 500 μm thick. The cleaving procedure will be described later.

The sample is then mounted on a 2° bevelling block with glycol resin. It is oriented so that the bevel lies along a crystallographic direction.

The abrasive slurry used is a suspension of 0.3 μm aluminum oxide particles in water at room temperature. The slurry is applied to a horizontal plate glass bevelling surface. The bevelling block with sample is gently placed into the slurry on the plate. Care must be taken to prevent edge chipping of the sample.

The bevel is formed by gently moving the block in the direction of the bevel edge. At the end of each stroke the block is lifted off the plate, bevel side first. Upon return to the starting position, the block is lowered gently onto the plate so that the bevelled edge makes contact last. No bevelling pressure is applied other than that provided by the 250g bevelling block. The procedure is schematically illustrated in Fig. 1.

A 1.4 mm long bevel representing a depth of approximately 35 μm is sufficient for ISS damage applied with 6 to 10 watts power for about one minute. The final bevel angle, which varies due to sample thickness variations, is determined by goniometer. This permits accurate depth calculations from the bevel angle.

2.1.2 Etching of Bevels

Bevel surfaces show only a few traces of the most severe ISS damage. A structure etch must be applied to make the extent of the damage visible.

A portion of a sample is shown before bevelling, after bevelling, and after etching in Figs. 2a, b, and c, respectively. Several severe damage sites are visible on

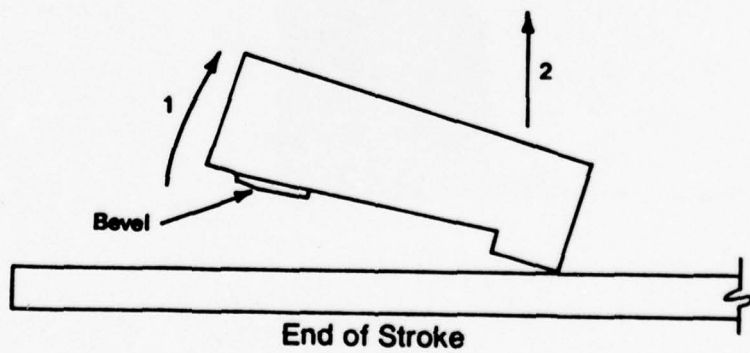
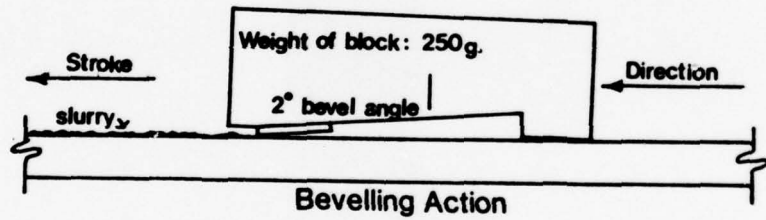
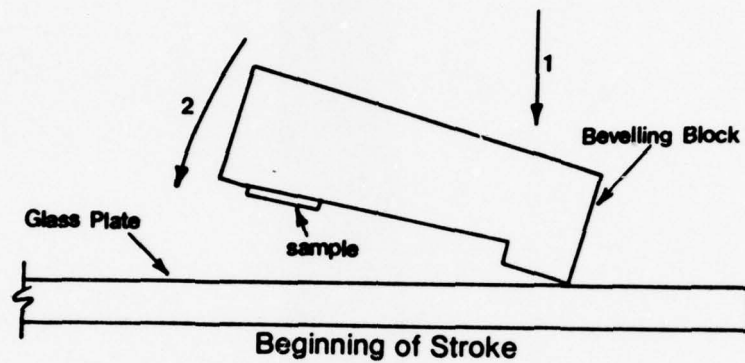


Fig. 1. Bevelling technique.

**Best
Available
Copy**

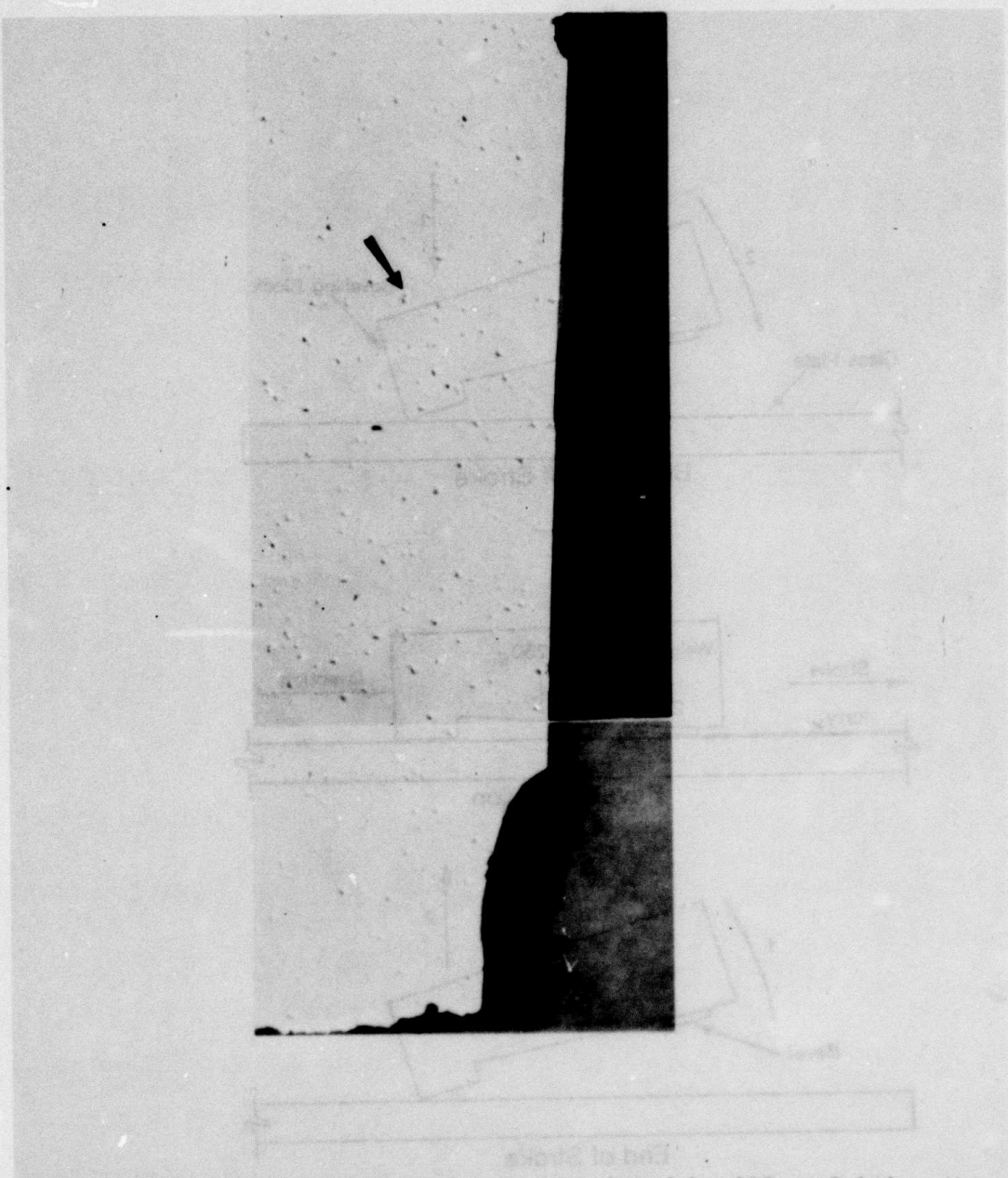


Fig. 2a. Microdamage in GaAs surface, induced by ISS at 6 1/4 watts for 60 sec. Arrow locates damage site visible in Fig. 2b.
Sample ID # 6.25/1/10-21. 46X magnification.

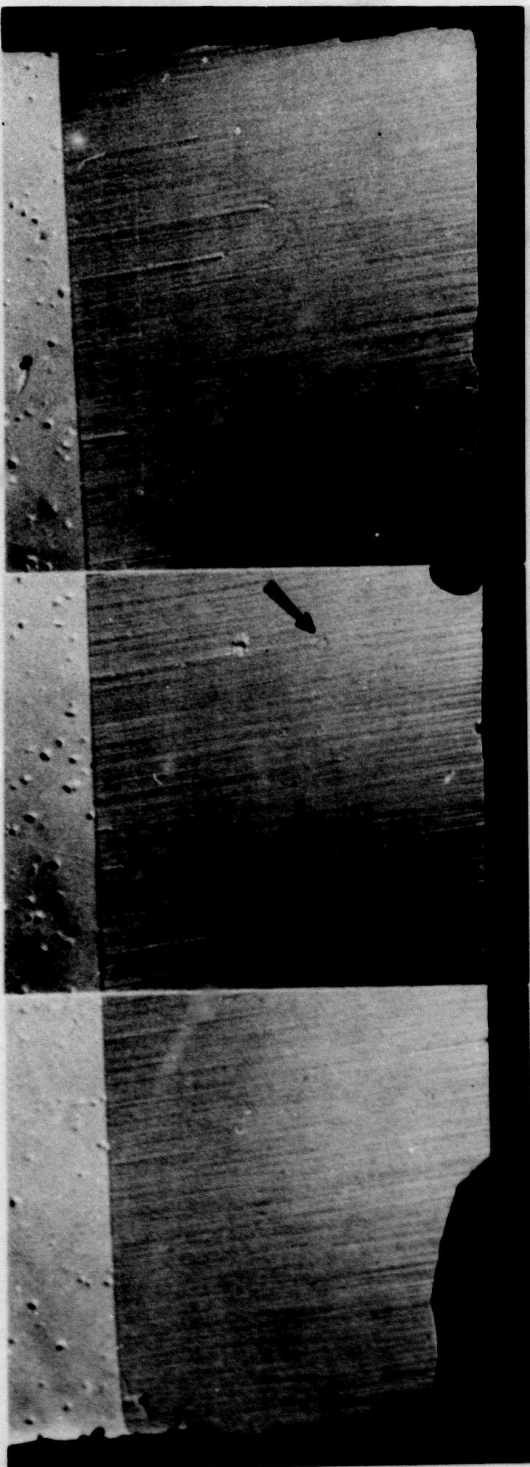


Fig. 2b. Same area as in Fig. 2a, bevelled at an angle of $1^{\circ} 19'$
46X magnification.

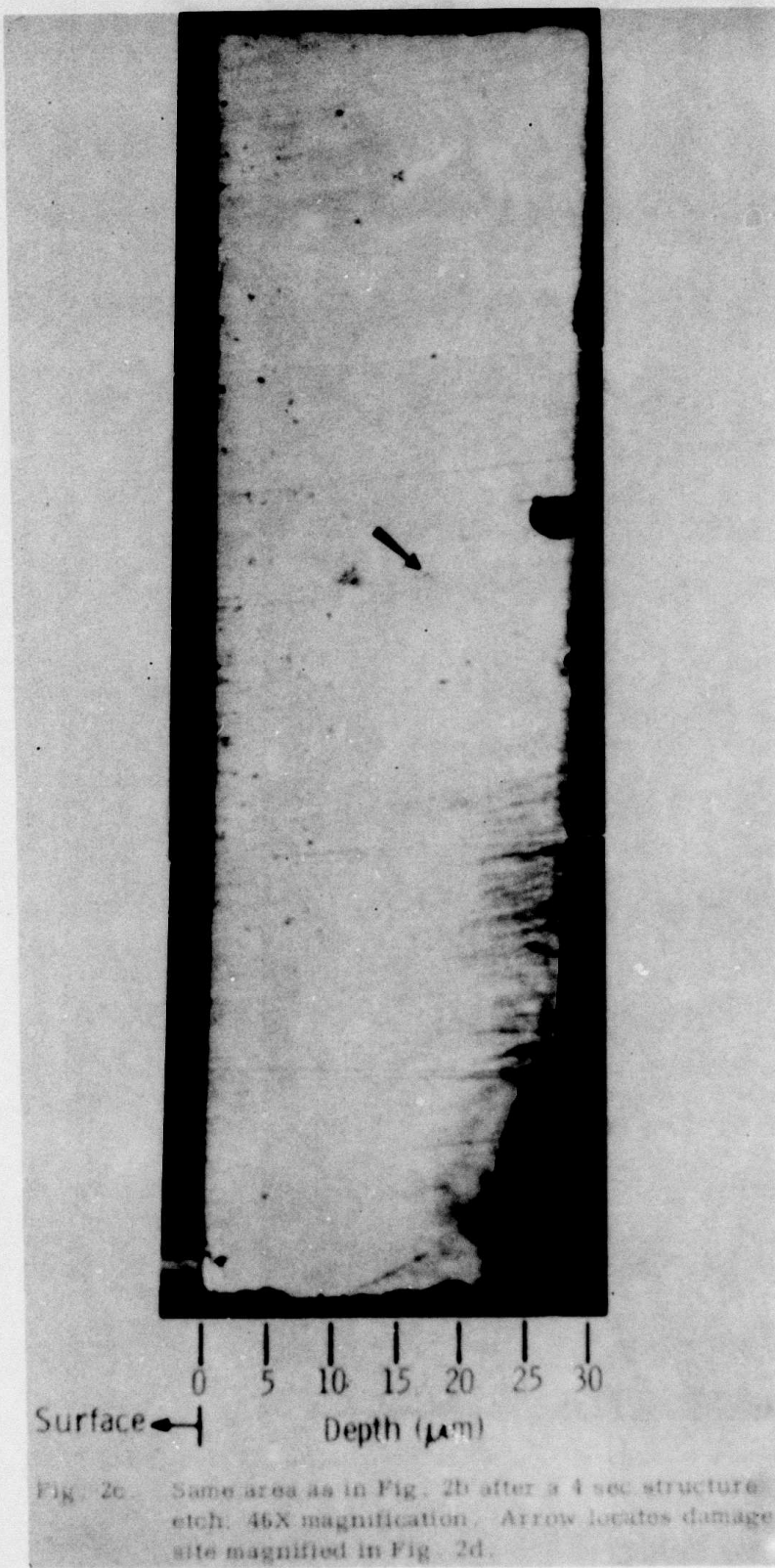


Fig. 2c. Same area as in Fig. 2b after a 4 sec structure etch. 46X magnification. Arrow locates damage site magnified in Fig. 2d.



Fig. 2d. Closeup view (320X magnification) of etch figure indicated by arrow in Fig. 2c due to damage site located by arrows in Figs. 2a and 2b.

the unetched bevel in Fig. 2b. An example is the site marked with an arrow on all three micrographs. In Fig. 2c large numbers of etch figures are seen outlining the damage sites not identifiable before etching.

The etch used for delineating the damage consists of equal parts of HNO_3 , HF and deionized water (3). The sample is held with teflon coated tweezers on the side opposite the bevel. It is dipped into the etching solution bevel up. The sample is held motionless in the solution for four seconds. Three seconds are required for etching action to start as evidenced by bubbling.

Etching time is controlled accurately with a foot switch actuated timer. The timer is started the instant the sample is dipped. It signals the end of the etching cycle with an audible signal. The sample is then withdrawn and immediately quenched in water.

2.1.3 Identification of Etched ISS Damage on Bevels

A band of damage delineated by the etching extends down from the intersection of the bevel with the sample surface (Fig. 2c).

In addition, scattered etch figures are seen farther down the bevel. Some of these may be due to other causes such as contamination, imbedded abrasive particles, or extraneous surface damage. Determination of the maximum depth of damage necessitates identification of these figures as ISS damage. This is accomplished by either one or both of two procedures. The questionable etch figures are first examined for typical appearance by high magnification light optical microscopy and scanning electron microscopy. Additional identification may be made, if necessary, by location correlation with micrographs of the area in question taken before bevelling. The closeup view of the etch figure shown in Fig. 2d reveals that it has the "typical" appearance. It can also be correlated with a damage site in Fig. 2a. Its location, 115 mm from end of bevel and 23 mm from edge of bevel measured on micrograph 2c, corresponds to that of a heavy damage site at a location measured similarly on micrograph 2a. The etch figure is thus identical as outlining ISS induced damage.

Some examples of etch figures typical for ISS damage are compared with etch figures due to extraneous causes in Fig. 3. Two low magnification (46X) micrographs showing sections of an etched bevel are given in Fig. 3a. The etch figures being compared are indicated by numbered arrows. They are

**Best
Available
Copy**

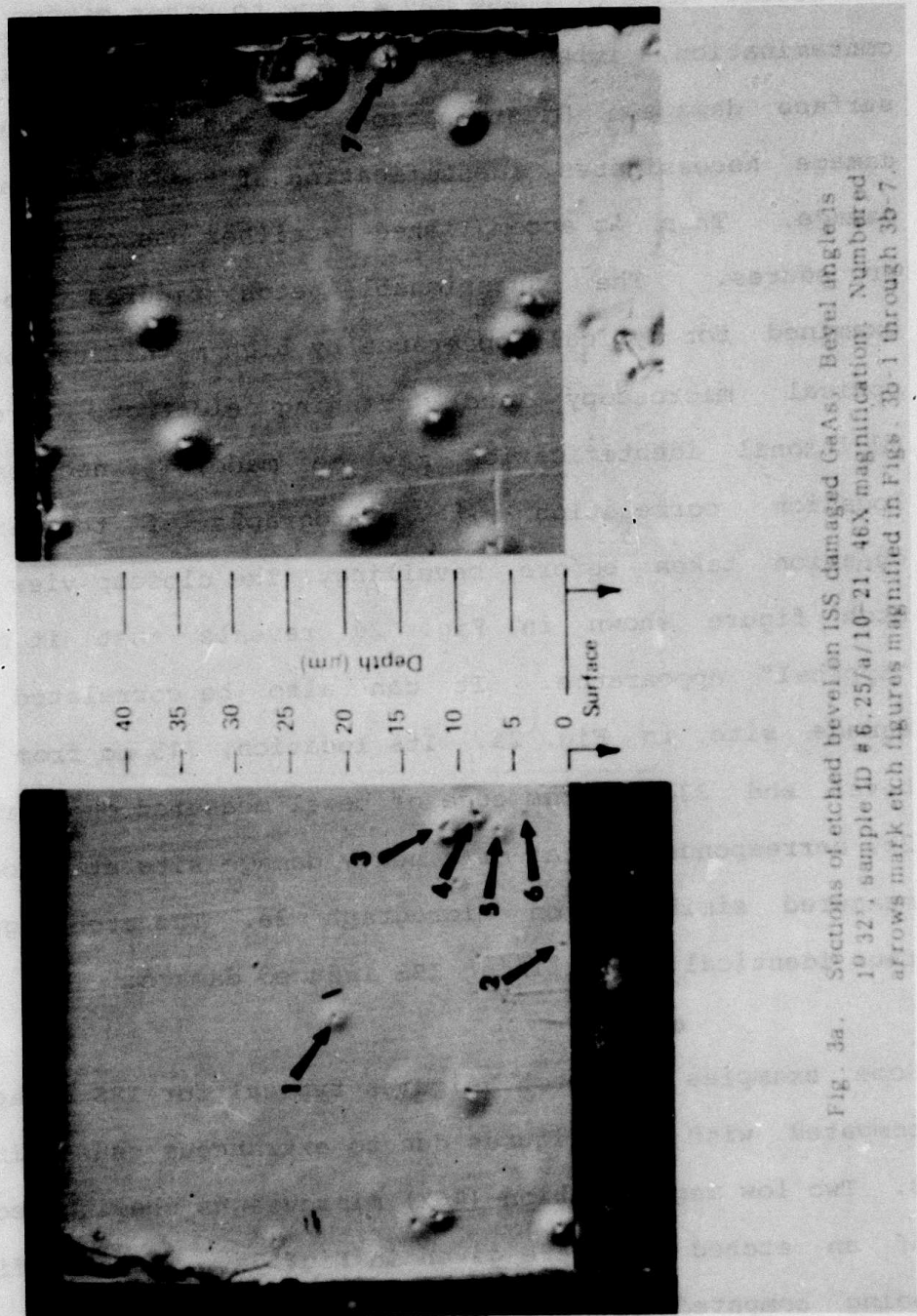


Fig. 3a. Sections of etched bevel on ISS damaged GaAs. Bevel angle is 10° 32'. sample ID # 6, 25/a/10-21, 46X magnification. Numbered arrows mark etch figures magnified in Figs. 3b-i through 3b-7.

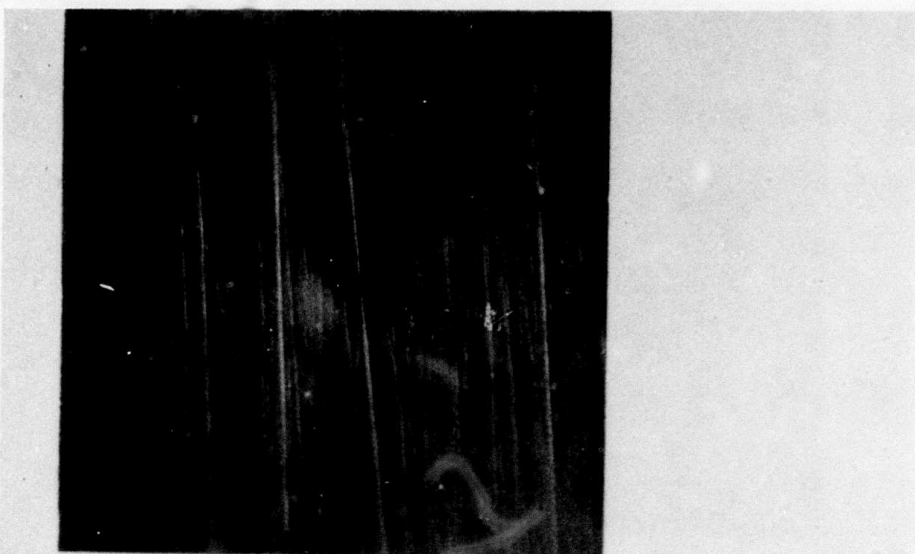


Fig. 3b-1. Etch figure not due to ISS damage.
855X magnification.

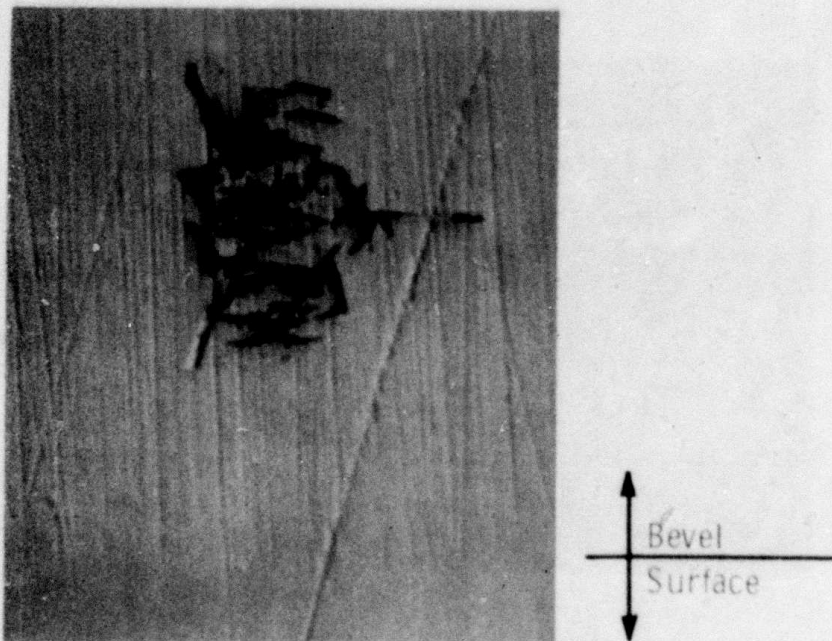


Fig. 3b-2. Etch figure due to ISS damage:
1390X magnification.



Light optical micrograph, 1390X magnification.



SEM micrograph, 4.7 KX magnification.

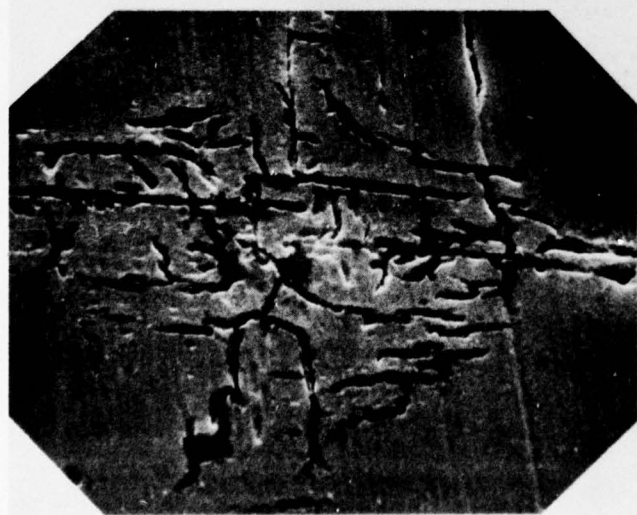
Fig. 3b-3. Particle on etched bevel.



Light optical micrograph;
900X magnification.

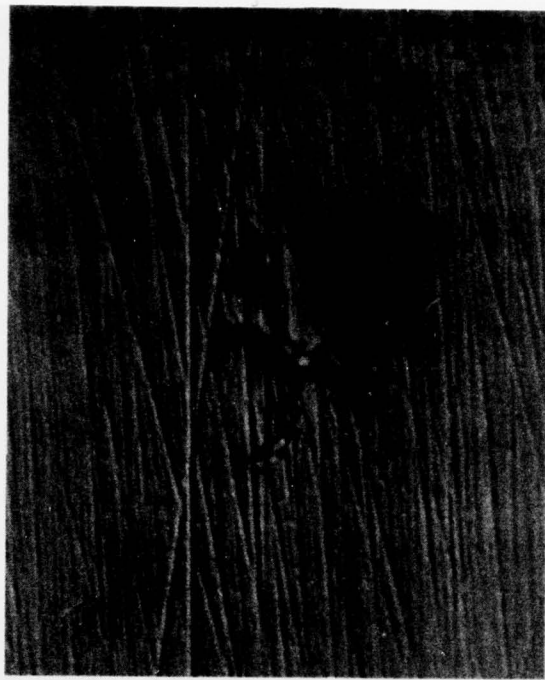


SEM micrograph; 940X magnification.

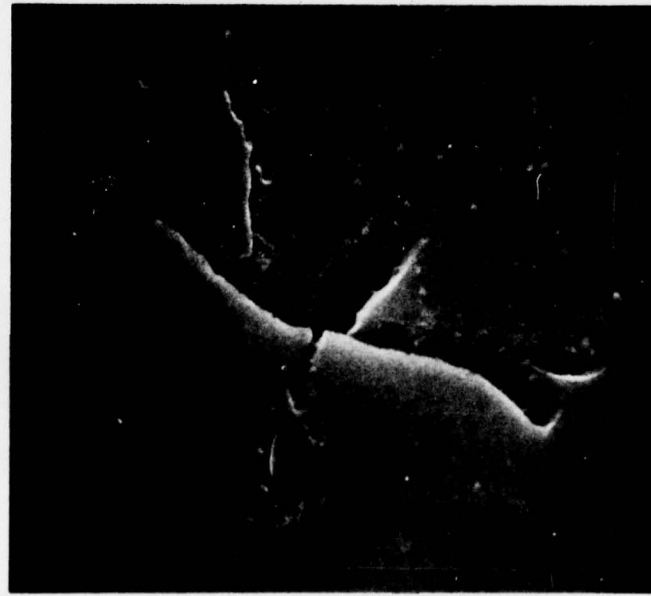


Central view of etch figure
shown above;
3.2KX magnification.

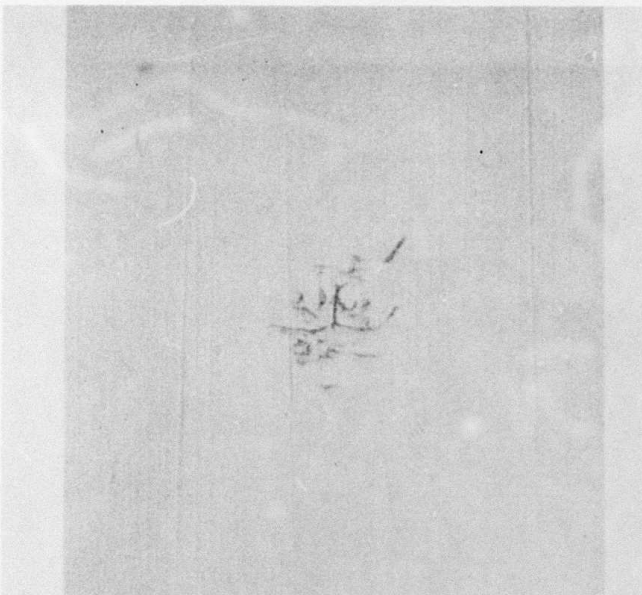
Fig. 3b-4. Etch figure due to ISS damage.



Light optical micrograph; 1390X magnification.



SEM micrograph showing broken edges on some grooves;
4.7KX magnification.



Light optical micrograph; 900X magnification.

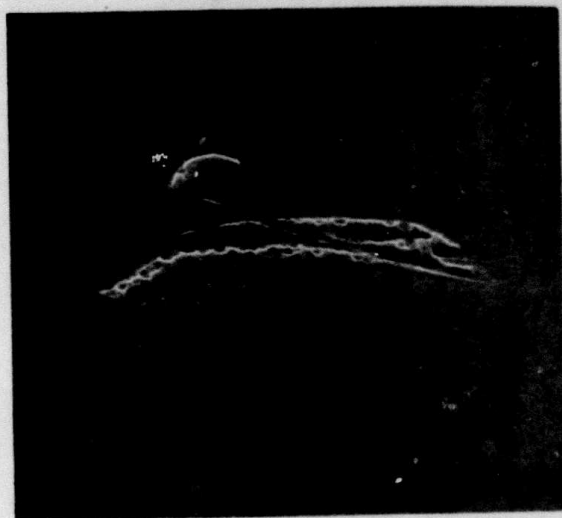


SEM micrograph; 3.2 KX magnification.

Fig. 3b-6. Etch figure typical of ISS damage.



Light optical micrograph; 855X magnification.



SEM micrograph; 900X magnification.

Fig. 3b-7. Etch figure not due to ISS damage. Possibly caused by surface contamination.

shown magnified in detail in Fig. 3b. Etch Figs. 1, 3, and 7 (Figs. 3b-1, 3b-3, and 3b-7) are not due to ISS induced damage. The remaining four etch figures are typical of etched ISS induced damage and are thus identified. The long etched out grooves are due to fractures and the short feathery ones are etched dislocation chains. Figures 3b-2, 3b-4, and 3b-6 are good examples. The two lower micrographs in Figs. 3b-4 are SEM recordings. The lower one gives a closeup view clearly showing the etched grooves. The lower micrograph in Figs. 3b-6 gives another such example. The upper edges of the fractures seen in the SEM micrograph of Figs. 3b-5 appear broken away. This may have occurred during bevelling.

Etch Fig. 1, at high magnification, is seen to be a shallow surface disturbance atypical of ISS damage. Etch Figs. 3 is identified in the SEM micrograph as a form protruding from the surface. It may be an imbedded aluminum oxide particle carried to its site in the abrasive slurry during bevelling. The SEM micrograph in the lower portion of Figs. 3b-7 shows that etch Fig. 7 has none of the typical etched grooves of ISS damage. It may be due to surface contamination.

2.2 Cleaving

2.2.1 Cleaving Procedure

The samples to be cleaved are placed on a sheet of filter paper with the polished side containing the damage facing down. The paper forms a resilient base. The edge of a glass slide is placed along the desired crystallographic direction and a slight pressure exerted until the sample cleaves. A clean and accurate cleavage plane is obtained by this method.

2.2.2 Identification of Damage Sites on Cleavage Plane

Damage sites on cleavage planes must be properly identified. This is to avoid errors which would occur if extraneous chipping and other non-ISS induced damage were included in depth of damage measurements.

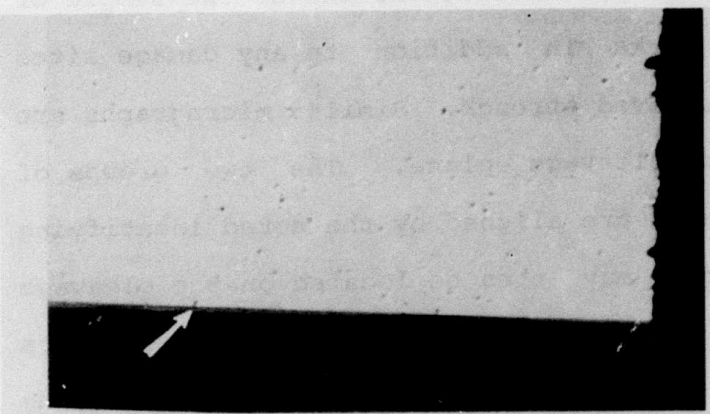
The area on the sample surface adjacent to the cleavage plane to be examined is photographed by light optical microscopy at low magnification (46X). In observing the fine surface fractures at the damage sites, considerably better contrast (and at lower magnification) is obtainable with light optical than with scanning electron microscopy.

These surface micrographs include the end of the sample or other identifying marks in addition to any damage sites which have been cleaved through. Similar micrographs are then taken of the cleavage plane. The two groups of micrographs or montages are aligned by the noted identifying marks. Damage sites may then be located on the cleavage plane visually or, if necessary, by linear measurements taken from the end of the sample, or from other identifying marks.

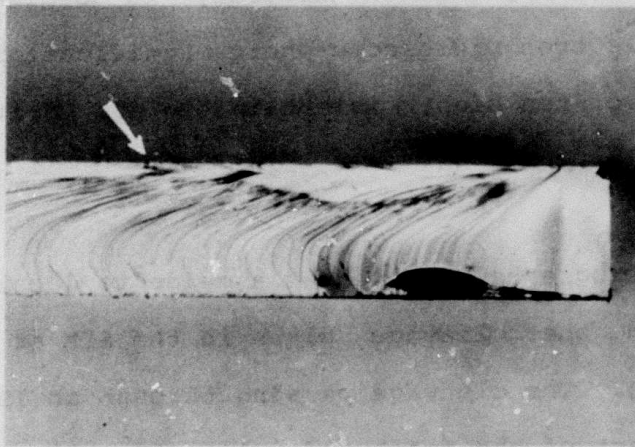
Damage depth measurements can be made on light optical micrographs of the cleavage plane at up to about 200X magnification. Considerably better accuracy is obtained with the scanning electron microscope where magnifications of more than a factor of ten higher is obtainable due to its great depth of field.

The light optical micrographs are used as a guide to locate the damage sites on the cleavage plane in the SEM at a similar magnification. The cleavage passing through an ISS damage site causes part of the fractured volume to collapse and fall out. This provides excellent contrast in the SEM and the sites are easily located for subsequent high magnification recording. The procedure is illustrated in Figs. 4.

**Best
Available
Copy**

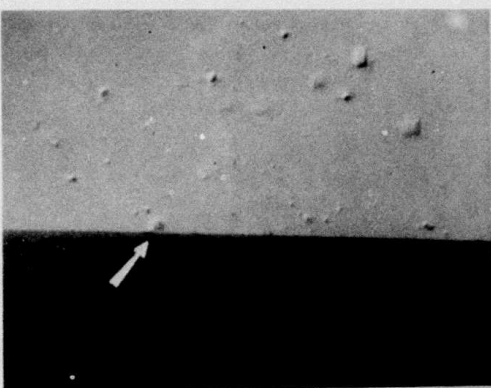


Surface; 46X magnification.

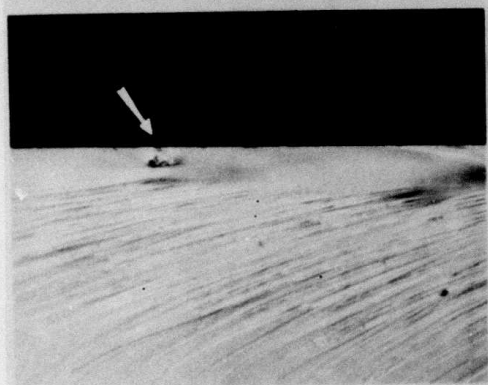


Cleavage plane; 46X magnification.

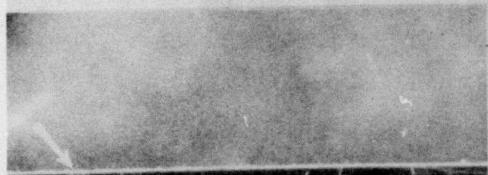
Fig. 4a. Cleaved, ISS damaged GaAs sample, sample ID # 6.25/1/10-21. Arrows indicate cleaved through damage site.



Light optical micrograph of surface;
167X magnification.



Light optical micrograph of cleavage plane;
167X magnification.



SEM micrograph of cleavage plane;
200X magnification.

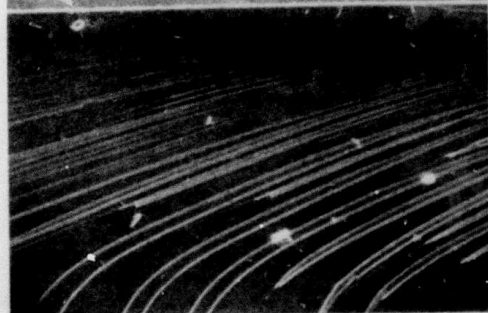


Fig. 4b. Magnified view of damage site shown in Fig. 4a for
location in SEM.

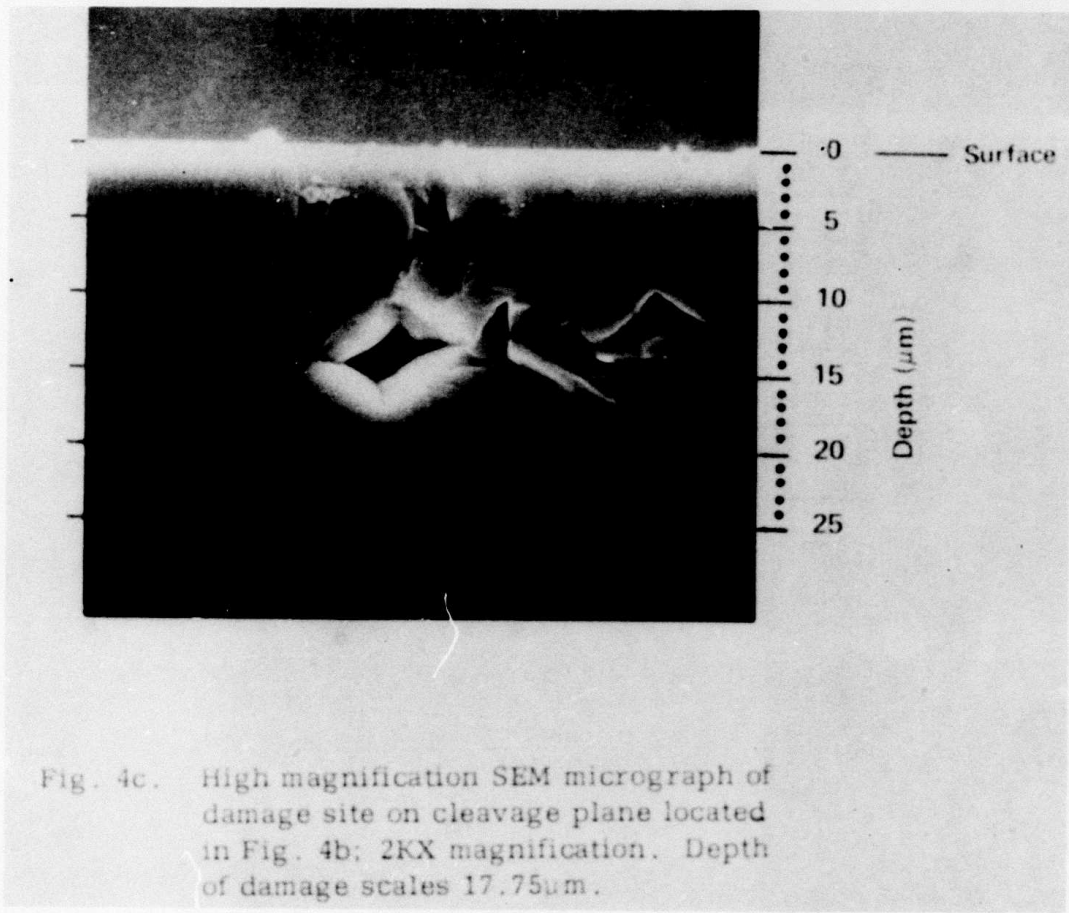


Fig. 4c. High magnification SEM micrograph of damage site on cleavage plane located in Fig. 4b; 2KX magnification. Depth of damage scales 17.75 μ m.

Figure 4a shows the surface of a cleaved sample in the top micrograph. The arrow points to a damage site which has been cleaved through. An edge view of the same area is given below the surface micrograph, with the damage site identified on the cleavage plane. Magnified views of the area of the damage site are given in Fig. 4b.

The edge view at the center is used as a guide to locate the damage site in the scanning electron microscope. A slightly more magnified scanning electron micrograph of the same area is given below. This shows where the damage site has been identified on the cleavage plane. Figure 4c shows the final scanning electron micrograph of the damage site in the cleavage plane taken at 2000X magnification. The cleavage plane is placed perpendicular to the electron beam for recording. This avoids fore-shortening and allows direct depth measurements from the micrograph.

3. RESULTS

The samples examined give an indication as to the depth of damage to be expected from 60 sec ISS runs at 6-1/4 to 10 watts power. The bevels showed a high damage density band reaching to a depth of about 10 μm . Maximum depth for individual damage sites ranged to over 27 μm . Table I below

gives the details for four bevels. The first number of the sample identification represents the driver input power in watts used for each run.

TABLE I. Depth of ISS Damage in GaAs as Measured on Bevels

Sample Identification	Bevel Angle	Maximum Damage Depth (μm)	Resistivity
6.25/a/10-21	$1^\circ 32'$	14.5	($> 10 \Omega\text{-cm}$)
6.25/c/10-21	$1^\circ 34'$	19.0	($> 10 \Omega\text{-cm}$)
6.25/l/10-21	$1^\circ 19'$	19.2	($> 10 \Omega\text{-cm}$)
10/10-22	$1^\circ 16'$	27.4	($\sim 0.001 \Omega\text{-cm}$)

Maximum depth measurements on bevels are made in the standard manner. The perpendicular distance from the bevel/surface intersect to the farthest delineated damage site on the bevel is measured directly on the micrograph.

The following equation is then applied:

$$d = \frac{10^3}{m} (L \tan \alpha)$$

where d = depth of damage in microns

L = distance measured on micrograph in millimeters

α = bevel angle (measured on goniometer)

m = magnification of micrograph

The maximum damage depth found by cleaving correlates well with that determined by the bevelling technique.

The damage sites cleaved through are located on the cleavage plane and are micrographed by SEM at 2000X magnification or higher. The depth is calculated from measurements made directly on the micrograph and the magnification.

Maximum depth of damage approaches 26 μm , which is in the same order of magnitude found with bevelling. Table II gives depths found on six cleavage planes. Driver input power is shown in Table I.

TABLE II. Depth of ISS Damage in GaAs as Measured on Cleavage Planes

Sample Identification	Maximum Damage Depth (μm)	Resistivity	Number of Sites Measured	Average Damage Depth (μm)
10/9-29	13.6	> 10 $\Omega\text{-cm}$	-	-
6.25/1/10-21 (plane a.)	17.8	> 10 $\Omega\text{-cm}$	-	-
10/10-22 (plane a.)	23.5	$\sim 0.001 \Omega\text{-cm}$	-	-
6.25/1/10-21 (plane b.)	25.8	> 10 $\Omega\text{-cm}$	8	19.3
10/10-22 (plane b.)	24.8	$\sim 0.001 \Omega\text{-cm}$	27	16.5
10/LD-784	15.3	0.00349 $\Omega\text{-cm}$	6	12.7

Damage on any given sample reaches a range of varying depths at different sites. This is due to the tungsten balls, in various trajectories, impacting with unequal force and impact angle.

4. CONCLUSION

ISS damage induced at 10 watts power, for 60 seconds, reaches a maximum depth approaching 30 μm . Most of the damage sites reach a depth of 10 μm . A decreasing number reaches deeper than 10 μm , and a small percentage reaches maximum depth of $\sim 30 \mu\text{m}$.

Resistivity does not appear to be a depth determining factor.

It might be expected that depth would vary somewhat with power settings and, due to repeated impacts, even with time. Tests indicate, however, that this may not be very significant within the limits of the experimental matrix described in Appendix II(a).

Two effective methods for determining ISS damage depth in GaAs have been developed. The methods, bevelling and cleaving, are complementary. Cleaving is more convenient,

but good accuracy requires use of a scanning electron microscope.

5. ACKNOWLEDGMENT

The bevelling technique was developed and all bevelling was done by Mr. Edward F. Gorey.

6. REFERENCES

1. ARPA Report No. 4, Contract No. DAHC-15-72-C-0274.
2. ARPA Report No. 6, Contract No. DAHC-15-72-C-0274.
3. A. F. Bogenschuetz, "Etching of Semiconductors", published by Carl Hanser Verlag, Munich, (1967).